IUEP-HEP-18-02

Higgs-boson-pair production $H(\to b\bar{b})H(\to \gamma\gamma)$ from gluon fusion at the HL-LHC and HL-100 TeV hadron collider

Jung Chang[1,2], Kingman Cheung[2,3,4], Jae Sik Lee[1,2,5], Chih-Ting Lu[4], and Jubin Park[5,1,2]
[1] *Department of Physics, Chonnam National University, 300 Yongbong-dong, Buk-gu, Gwangju, 500-757, Republic of Korea*
[2] *Physics Division, National Center for Theoretical Sciences, Hsinchu, Taiwan*
[3] *Division of Quantum Phases and Devices, School of Physics, Konkuk University, Seoul 143-701, Republic of Korea*
[4] *Department of Physics, National Tsing Hua University, Hsinchu 300, Taiwan*
[5] *Institute for Universe and Elementary Particles, Chonnam National University, 300 Yongbong-dong, Buk-gu, Gwangju, 500-757, Republic of Korea*

(Dated: July 15, 2019)

We perform the most up-to-date comprehensive signal-background analysis for Higgs-pair production in $HH \to b\bar{b}\gamma\gamma$ channel at the HL-LHC and HL-100 TeV hadron collider, with the goal of probing the self-coupling λ_{3H} of the Higgs boson which is normalized to its Standard Model value of 1. We simulate all the standard-model signal and background processes and emphasize that the $ggH(\to \gamma\gamma)$ background has been overlooked in previous studies. We find that even for the most promising channel $HH \to b\bar{b}\gamma\gamma$ at the HL-LHC with a luminosity of 3000 fb^{-1}, the significance is still not high enough to establish the Higgs self-coupling at the standard model (SM) value. Instead, we can only constrain the self-coupling to $-1.0 < \lambda_{3H} < 7.6$ at 95% confidence level after considering the uncertainties associated with the top-Yukawa coupling and the estimation of backgrounds. Here we also extend the study to the HL-100 TeV hadron collider. With a luminosity of 3 ab^{-1}, we find there exists a bulk region of $2.6 \lesssim \lambda_{3H} \lesssim 4.8$ in which one cannot pin down the trilinear coupling. Otherwise one can measure the coupling with a high precision. At the SM value, for example, we show that the coupling can be measured with about 20 % accuracy. While assuming 30 ab^{-1}, the bulk region reduces to $3.1 \lesssim \lambda_{3H} \lesssim 4.3$ and the trilinear coupling can be measured with about 7 % accuracy at the SM value.

arXiv:1804.07130v3 [hep-ph] 15 Jul 2019

I. INTRODUCTION

Origin of mass is the most important question that one would ask for our existence. This is related to the mechanism involved in electroweak symmetry breaking (EWSB), which is believed to give masses to gauge bosons and fermions. The simplest implementation in our standard model (SM) is to introduce a Higgs doublet field, whose non-vanishing vacuum expectation value causes EWSB [1]. The by-product is a neutral scalar Higgs boson, which was eventually discovered in July 2012 [2]. After accumulating enough data at the end of 8 TeV runs, the scalar boson is best described by the SM Higgs boson [3], in which the couplings to gauge bosons are confirmly established and those to fermions started to fall in the ball-park of the SM values. However, the SM Higgs boson can hardly constitute a complete theory because of, for example, the gauge hierarchy problem.

The current measurements of the Higgs-boson properties mainly concern the couplings of the Higgs boson to the SM particles. There is no *a priori* reason why the EWSB sector simply contains only one Higgs doublet field. Indeed, many extensions of the EWSB sector consist of more Higgs fields. Until now there is no information at all about the self-couplings of the Higgs boson, which depends on the dynamics of the EWSB sector. The self-couplings of the Higgs boson are very different among the SM, two-Higgs doublet models (2HDM), and MSSM. One of the probes of Higgs self-coupling is Higgs-boson-pair production at the LHC [4–6]. There have been a large number of works in literature on Higgs-pair production in the SM [7], in model-independent formalism [8], in models beyond the SM [9], and in SUSY [10].

The predictions for various models are largely different such that the production rates can give valuable information on the self-coupling λ_{3H}. In the SM, Higgs-pair production receives contributions from both the triangle and box diagrams, which interfere with each other. It is only the triangle diagram that involves the Higgs self-trilinear coupling λ_{3H}, yet the top-Yukawa coupling appears in both triangle and box diagrams. Therefore, we have to disentangle the triangle diagram from the box diagram in order to probe the Higgs trilinear coupling. In Ref. [11], we pointed out that the triangle diagram, with s-channel Higgs propagator, is more important at low invariant-mass region than the box diagram. Thus, the Higgs-boson pair from the triangle diagram tends to have lower invariant mass, and therefore the opening angle in the decay products of each Higgs boson tends to be larger than that from the box diagram. Indeed, the opening angle separations $\Delta R_{\gamma\gamma}$ and ΔR_{bb} between the decay products of the Higgs-boson pair are very useful variables to disentangle the two sources. However, in Ref. [11] we only assumed some level of signal uncertainties to evaluate the sensitivity to the parameter space of self-coupling λ_{3H} and the top-Yukawa coupling g_t^S, without calculating all the other SM backgrounds, e.g., jet-fake backgrounds, single Higgs associated backgrounds, and non-resonant backgrounds.

In this work, we perform the most up-to-date comprehensive signal-background analysis for Higgs-pair production through gluon fusion and the $HH \to b\bar{b}\gamma\gamma$ decay channel. For other production and decay channels and some combined analyses, see Refs. [12]. We simulate the signal and all background processes using simulation tools as sophisticated as what experimentalists use. The signal subprocess is $gg \to HH \to b\bar{b}\gamma\gamma$ with various values for λ_{3H}. The background includes $t\bar{t}$, $t\bar{t}\gamma$, single Higgs associated backgrounds (e.g. ZH, $t\bar{t}H$, $b\bar{b}H$, ggH followed by $H \to \gamma\gamma$), and non-resonant or jet-fake backgrounds (e.g. $b\bar{b}\gamma\gamma$, $b\bar{b}j\gamma$, $b\bar{b}jj$, $jj\gamma\gamma$, etc). We found a set of useful selection cuts to reduce the backgrounds. We express the sensitivity that can be achieved in terms of significance. We find that even for the most promising channel $HH \to b\bar{b}\gamma\gamma$ at the HL-LHC, the significance is still not high enough to establish the Higgs self-coupling at the SM value, though the self-coupling can be constrained to the range $0 < \lambda_{3H} < 7.1$ at 95% confidence level (CL) with an integrated luminosity of 3000 fb^{-1}. Taking account of the uncertainties associated with the top-Yukawa coupling and the estimation of backgrounds, we have found that the 95% CL region broadens into $-1.0 < \lambda_{3H} < 7.6$. We also extend the analysis to the HL-100 TeV hadron collider. With a luminosity of 3 ab^{-1}, we find a bulk region of $2.6 \lesssim \lambda_{3H} \lesssim 4.8$ in which one cannot pin down the trilinear coupling. Otherwise one can measure the coupling with a high precision. At the SM value, for example, we show that the coupling can be measured with about 20% accuracy. While assuming 30 ab^{-1}, the bulk region reduces to $3.1 \lesssim \lambda_{3H} \lesssim 4.3$ and the trilinear coupling can be measured with about 7 % accuracy at the SM value. This is the main result of this work.

This work has a number of improvements over our previous and other works in literature, summarized as follows.

1. We have included all the backgrounds, including $t\bar{t}$ related ones, single Higgs associated production processes, non-resonant backgrounds, and jet-fake backgrounds. Furthermore we would like to emphasize that we have implemented through detector simulations of all the backgrounds.

2. While implementing all the relevant signal and background simulations, we find that the $ggH(\to \gamma\gamma)$ background is possibly very important and has been overlooked in previous studies. Note that the similar observation has been recently made by the authors of Ref. [13].

3. For the signal, since the signal distributions behave differently for different λ_{3H}, we evaluate the selection efficiency separately for each λ_{3H} to properly cover the viable range of the non-standard values of λ_{3H}.

4. At the HL-LHC, we firstly take into account the impact of the uncertainty associated with the top-Yukawa coupling on 95% CL sensitivity. We find that, especially, the lower boundary of the 95% CL region of λ_{3H} significantly varies upon the expected precision of the top-quark Yukawa coupling in the HL-LHC era.

5. Taking account of all the backgrounds known up to date and devising a *new* set of selection cuts, we have most reliably estimated the potential reach of HL-100 TeV hadron collider for a broad range of λ_{3H}.

6. At the HL-100 TeV collider, we find there is a two-fold ambiguity in λ_{3H} which could be lifted up by exploiting several kinematical distributions. We also find that there exists a bulk region in which it would be difficult to establish the λ_{3H} coupling even at the HL-100 TeV collider.

The organization is as follows. In the next section, we briefly describe the effective Lagrangian for Higgs-pair production. In Sec. III, we describe the signal and background processes and simulation tools. We also present the distributions, selection cuts, cut flows of signal and backgrounds, and significance for the HL-LHC. Section IV is dedicated to the case of HL-100 TeV hadron collider. In Sec. V, we examine the impact of the NLO corrections considering full top-quark mass dependence, the effect of using a modern PDF set to include the LHC data on PDF, and how the investigation of the uncertainties involved in the matching procedures affects the 95% CL sensitivity region of λ_{3H}. We discuss and conclude in Sec. VI. We put some extra distributions and cut flow tables, which can be ignored in the first reading, into the appendices A and B. Appendix C, on the other hand, gives the details for the procedures employed in the matching in calculating the cross sections of the non-resonant backgrounds, as well as their uncertainties.

II. EFFECTIVE LAGRANGIAN

The contributing Feynman diagrams for Higgs-boson-pair production via gluon fusion include a triangle diagram with a Higgs-boson propagator and a box diagram with colored particles running in them. The relevant couplings involved are top-Yukawa and the Higgs trilinear self coupling, which are given in this Lagrangian:

$$-\mathcal{L} = \frac{1}{3!}\left(\frac{3M_H^2}{v}\right)\lambda_{3H}\,H^3 \; + \; g_t^S\,\frac{m_t}{v}\,\bar{t}\,t\,H \tag{1}$$

In the SM, $\lambda_{3H} = g_t^S = 1$. The differential cross section for the process $g(p_1)g(p_2) \to H(p_3)H(p_4)$ was obtained in Ref. [14] as

$$\frac{d\hat{\sigma}(gg \to HH)}{d\hat{t}} = \frac{G_F^2\alpha_s^2}{512(2\pi)^3}\left[\left|\lambda_{3H}g_t^S D(\hat{s})F_\triangle^S + (g_t^S)^2F_\Box^{SS}\right|^2 + \left|(g_t^S)^2G_\Box^{SS}\right|^2\right] \tag{2}$$

where

$$D(\hat{s}) = \frac{3M_H^2}{\hat{s} - M_H^2 + iM_H\Gamma_H} \tag{3}$$

and $\hat{s} = (p_1+p_2)^2$, $\hat{t} = (p_1-p_3)^2$, and $\hat{u} = (p_2-p_3)^2$ with $p_1+p_2 = p_3+p_4$. The loop functions $F_\triangle^S = F_\triangle$, $F_\Box^{SS} = F_\Box$, and $G_\Box^{SS} = G_\Box$ with $F_{\triangle,\Box}$ and $G_\Box$ given in Appendix A.1 of Ref. [14]. In the heavy quark limit, one may have

$$F_\triangle^S = +\frac{2}{3} + \mathcal{O}(\hat{s}/m_Q^2)\,, \quad F_\Box^{SS} = -\frac{2}{3} + \mathcal{O}(\hat{s}/m_Q^2)\,, \quad G_\Box^{SS} = \mathcal{O}(\hat{s}/m_Q^2) \tag{4}$$

leading to large cancellation between the triangle and box diagrams.

The production cross section normalized to the corresponding SM cross section, with or without cuts, can be parameterized as follows:

$$\frac{\sigma^{\rm LO}(gg \to HH)}{\sigma^{\rm LO}_{\rm SM}(gg \to HH)} = c_1(s)\,\lambda_{3H}^2\,(g_t^S)^2 + c_2(s)\,\lambda_{3H}\,(g_t^S)^3 + c_3(s)\,(g_t^S)^4 \tag{5}$$

where the numerical coefficients $c_{1,2,3}(s)$ depend on s and experimental selection cuts. Numerically, $c_1(s), c_2(s), c_3(s)$ are $0.263\,, -1.310\,, 2.047$ at 14 TeV and $0.208\,, -1.108\,, 1.900$ at 100 TeV [11]. Upon our normalization, the ratio should be equal to 1 when $g_t^S = \lambda_{3H} = 1$, or $c_1(s) + c_2(s) + c_3(s) = 1$. The coefficients $c_1(s)$ and $c_3(s)$ are for the contributions from the triangle and box diagrams, respectively, and the coefficient $c_2(s)$ for the interference between them. Once we have the coefficients c_i the cross sections can be easily obtained for any combinations of couplings.

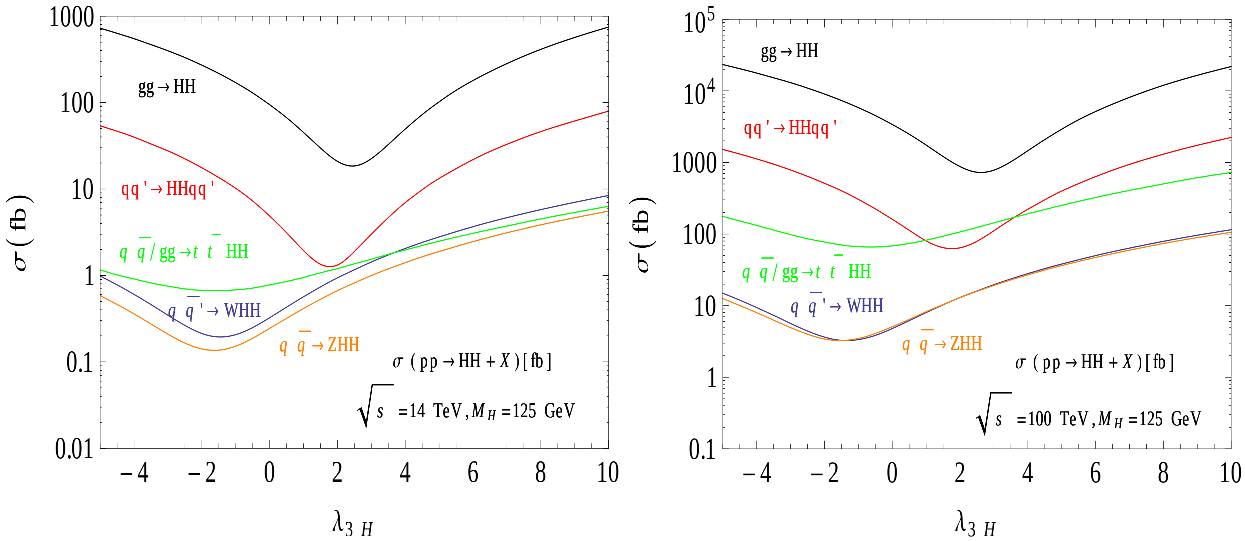

FIG. 1. Production cross sections for various channels for HH production at $\sqrt{s} = 14$ TeV (left) and $\sqrt{s} = 100$ TeV (right). The `NNPDF2.3LO` PDF set is used.

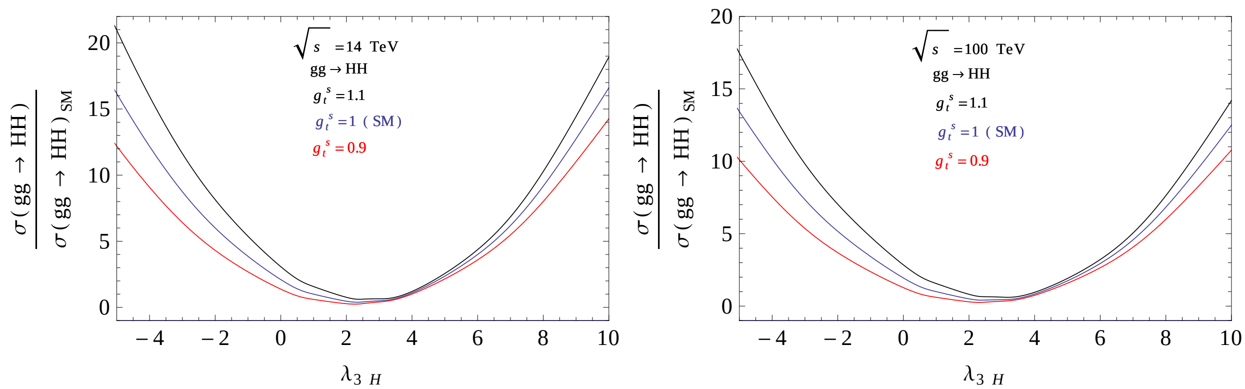

FIG. 2. Ratio of cross sections $\sigma(gg \to HH)/\sigma(gg \to HH)_{\rm SM}$ versus λ_{3H} taking account of 10% uncertainty of the top-Yukawa coupling: $g_t^S = 1.1$ (black), 1 (blue), and 0.9 (red) for $\sqrt{s} = 14$ TeV (left) and $\sqrt{s} = 100$ TeV (right).

To get a feeling for the size of the cross sections that we are considering, we show the total production cross sections for various HH production channels in Fig. 1. At 14 TeV, the SM cross sections $\sigma(gg \to HH) = 45.05$ fb [15], $\sigma(qq' \to HHqq') = 1.94$ fb [16], $\sigma(q\bar{q}(') \to VHH = 0.567(V = W^\pm)\,/0.415(V = Z)$ fb [17], and $\sigma(gg/q\bar{q} \to t\bar{t}HH) = 0.949$ fb [16] are calculated at NNLO+NNLL, NLO, NNLO, and NLO, respectively [18]. The 100 TeV cross sections $\sigma(gg \to HH) = 1749$ fb, $\sigma(qq' \to HHqq') = 80.3$ fb, $\sigma(q\bar{q}(') \to VHH = 8.00(V = W^\pm)\,/8.23(V = Z)$ fb, and $\sigma(gg/q\bar{q} \to t\bar{t}HH) = 82.1$ fb are calculated at the same orders as at 14 TeV [19, 20]. From Fig. 1, it is clear that the gluon fusion into HH gives the largest cross sections independently of λ_{3H} with its minimum occurring at $\lambda_{3H} \simeq 2.5$. From now on we shall focus on the gluon fusion mechanism. We show the ratio of the cross sections for the $gg \to HH$ process as a function of λ_{3H} in Fig. 2, in which we also indicate the effects of allowing the top-Yukawa coupling to have $\pm 10\%$ uncertainty or $\delta g_t^S = \pm 0.1$. At the HL-LHC, the expected precision of measurement of the top-quark Yukawa coupling is 10% [21]. Currently, without knowing the absolute value of the top-quark Yukawa coupling no better than 10% precision, we also consider the $\delta g_t^S = \pm 10\%$ effect at 100 TeV though the expected uncertainty is 1% at the 100-TeV pp colliders.

III. SIMULATIONS, EVENT SELECTIONS, AND ANALYSIS AT THE 14 TEV HL-LHC

Our goal is to disentangle the effects of trilinear Higgs coupling, which is present in the triangle diagram, in Higgs-pair production. We focus on the decay channel $HH \to b\bar{b}\gamma\gamma$, in which the final state consists of a pair of b quarks

TABLE I. Monte Carlo samples used in Higgs-pair production analysis $H(\to b\bar{b})H(\to\gamma\gamma)$, and the corresponding codes for the matrix-element generation, parton showering, and hadronization. The third (fourth) column shows their cross section times branching ratio (the order in perturbative QCD of the cross section calculation applied), and the final column shows their PDF set used in the simulation. For the generation of non-resonant and $t\bar{t}\gamma$ backgrounds, some pre-selection cuts are applied at the parton level in order to remove the divergence associated with the photons or jets, see Eq. (6). Note that, except the $ggH(\to\gamma\gamma)$ and $t\bar{t}$ backgrounds which are generated at NLO, all the signal and backgrounds are generated at LO and normalized to the cross sections computed at the accuracy denoted in 'Order in QCD'.

Signal					
Signal process		Generator/Parton Shower	$\sigma\cdot BR$ [fb]	Order in QCD	PDF used
$gg\to HH\to b\bar{b}\gamma\gamma$ [18]		`MG5_aMC@NLO/PYTHIA8`	0.119	NNLO +NNLL	NNPDF2.3LO
Backgrounds					
Background(BG)	Process	Generator/Parton Shower	$\sigma\cdot BR$ [fb]	Order in QCD	PDF used
Single-Higgs associated BG [18]	$ggH(\to\gamma\gamma)$	`POWHEG-BOX/PYTHIA6`	1.20×10^2	NNNLO	`CT10`
	$t\bar{t}H(\to\gamma\gamma)$	`PYTHIA8/PYTHIA8`	1.37	NLO	
	$ZH(\to\gamma\gamma)$	`PYTHIA8/PYTHIA8`	2.24	NLO	
	$b\bar{b}H(\to\gamma\gamma)$	`PYTHIA8/PYTHIA8`	1.26	NLO	
Non-resonant BG	$b\bar{b}\gamma\gamma$	`MG5_aMC@NLO/PYTHIA8`	1.40×10^2	LO	`CTEQ6L1`
	$c\bar{c}\gamma\gamma$	`MG5_aMC@NLO/PYTHIA8`	1.14×10^3	LO	
	$jj\gamma\gamma$	`MG5_aMC@NLO/PYTHIA8`	1.62×10^4	LO	
	$b\bar{b}j\gamma$	`MG5_aMC@NLO/PYTHIA8`	3.67×10^5	LO	
	$c\bar{c}j\gamma$	`MG5_aMC@NLO/PYTHIA8`	1.05×10^6	LO	
	$b\bar{b}jj$	`MG5_aMC@NLO/PYTHIA8`	4.34×10^8	LO	
	$Z(\to b\bar{b})\gamma\gamma$	`MG5_aMC@NLO/PYTHIA8`	5.17	LO	
$t\bar{t}$ and $t\bar{t}\gamma$ BG ($\geq$ 1 lepton)	$t\bar{t}$ [22]	`POWHEG-BOX/PYTHIA8`	5.30×10^5	NNLO +NNLL	`CT10`
	$t\bar{t}\gamma$ [23]	`MG5_aMC@NLO/PYTHIA8`	1.60×10^3	NLO	`CTEQ6L1`

and a pair of photons reconstructed at the invariant mass around the Higgs-boson mass ($M_H\simeq 125$ GeV). We shall vary the value for the trilinear coupling λ_{3H} between -5 and 10 to visualize the effects of λ_{3H}. The backgrounds then include

- single-Higgs associated production, such as ggH, $t\bar{t}H$, ZH, $b\bar{b}H$ followed by $H\to\gamma\gamma$,
- non-resonant backgrounds and jet-fake backgrounds, such as $b\bar{b}\gamma\gamma$, $c\bar{c}\gamma\gamma$, $jj\gamma\gamma$, $b\bar{b}j\gamma$, $c\bar{c}j\gamma$, $b\bar{b}jj$, and $Z\gamma\gamma\to b\bar{b}\gamma\gamma$,
- $t\bar{t}(\geq 1$ lepton) and $t\bar{t}\gamma(\geq 1$ lepton) backgrounds .

All the signal and backgrounds are summarized in Table I, together with the information of the corresponding event generator, the cross section times the branching ratio ($\sigma\cdot BR$), the order in QCD for the calculation of $\sigma\cdot BR$, and the Parton Distribution Function (PDF) used.

A. Parton-level event generations and detector simulations

Parton-level events for the backgrounds $\big(b\bar{b}\gamma\gamma$, $c\bar{c}\gamma\gamma$, $jj\gamma\gamma$, $b\bar{b}j\gamma$, $c\bar{c}j\gamma$, $b\bar{b}jj$, $t\bar{t}\gamma$, and $Z(\to b\bar{b})\gamma\gamma\big)$ and for the signal $\big($with $-5\leq\lambda_{3H}\leq 10\big)$ are generated with **`MadGraph5_aMC@NLO`** (**`MG5_aMC@NLO`**) [24]. Backgrounds for gluon fusion and top-quark pair are generated with **`POWHEG BOX`** [25]. The single-Higgs associated backgrounds for $t\bar{t}H(\to\gamma\gamma), ZH(\to\gamma\gamma), b\bar{b}H(\to\gamma\gamma)$ are generated with **Pythia8** [26]. Here we would like to provide more detailed information on the parton-level generation of signal and background events. The signal cross sections are calculated with the adjustable Higgs self-coupling in UFO format [27] and events are generated in the loop induced mode [28]. The **`MadSpin`** code [29] is then employed to let the Higgs-boson pair decay into $b\bar{b}\gamma\gamma$. Further on the parton-level generation of non-resonant and $t\bar{t}\gamma$ backgrounds, the following pre-selection cuts at parton level are imposed in order to avoid any divergence in the parton-level calculations [30]:

$$\begin{aligned} P_{T_j} > 20 \;\; \text{GeV},\; P_{T_b} > 20 \;\; \text{GeV},\; P_{T_\gamma} > 25 \;\; \text{GeV},\; P_{T_l} > 10 \;\; \text{GeV}, \\ |\eta_j| < 5,\; |\eta_\gamma| < 2.7,\; |\eta_l| < 2.5,\; \Delta R_{jj,ll,\gamma\gamma,\gamma j,jl,\gamma l} > 0.4, \\ M_{jj} > 25 \text{ GeV},\; M_{bb} > 45 \text{ GeV},\; 60 < M_{\gamma\gamma} < 200 \text{ GeV}. \end{aligned} \tag{6}$$

For parton showering, hadronization, and decays of unstable particles, **Pythia8**[26] is used both for signal and backgrounds. Finally, fast detector simulation and analysis at the HL-LHC are performed using **Delphes3** [31] with the ATLAS template. In the template, we use the expected performance for photon efficiency, photon fake rates, b-jet tagging efficiency, and b-jet fake rates obtained with a mean pile-up $\langle\mu\rangle = 200$ (see Refs. [30, 32]). For the photon efficiency, we use the P_T-dependent formula

$$\epsilon_\gamma = 0.888 * \tanh(0.01275 * P_{T_\gamma}/\text{GeV})\,,$$

which we obtain by fitting to the ATLAS simulation results. At $P_{T_\gamma} \sim 50$ GeV, $\epsilon_\gamma \sim 50\%$ as in Ref. [30] and it approaches $\epsilon_\gamma \sim 85\%$ in the saturation region of the curve, at $P_{T_\gamma} \sim 150$ GeV to be specific, being consistent with ATLAS simulation [32]. The photon fake rates are taken from Ref. [30]: $P_{j\to\gamma} = 5\times 10^{-4}$ and $P_{e\to\gamma} = 2\%\,(5\%)$ in the barrel (endcap) region. The b-jet tagging efficiency ϵ_b depends on P_T and η of b jet and we have fully considered its P_T and η dependence, see Fig.7(b) of Ref. [32]. The charm-jet fake rate $P_{c\to b}$ depends on ϵ_b and, accordingly, on P_T and η of c jet. For the multi-variate MV1 b-tagging algorithm taken in our analysis, $P_{c\to b} \sim 1/5$ when $\epsilon_b = 0.7$ and it approaches 1 as $\epsilon_b \to 1$ [33]. In our simulation, the P_T and η dependence of $P_{c\to b}$ is also considered. For the light-jet fake rate, we are taking $P_{j\to b} = 1/1300$ [30]. Incidentally, we have also considered the energy loss due to the b momentum reconstruction from the b-tagged jet and set the jet-energy scale using the scaling formula [31]

$$\sqrt{\frac{(3.0 - 0.2|\eta_b|)^2}{P_{T_b}/\text{GeV}} + 1.27}$$

where the factor 1.27 is tuned to get a correct peak position at M_H in the invariant mass distribution of a b-quark pair in the signal process.

In this study, we do not include the pile-up effects into our simulation. There are a couple of reasons for this. First, it is expected that the pile-up effects can be dealt with by the upgraded event trigger in future, and its overall effect could be negligible in the channel of our interests [1]. More importantly, by imposing a narrow $M_{\gamma\gamma}$ invariant mass window cut in event selection, we could eventually obtain similar results independently of including the pile-up effects. This is because pile-up causes the stronger impact on photons than on b-jets and the soft fake photons from pile-up jets make the width of $M_{\gamma\gamma}$ peak wider. Incidentally, we also have checked that the simulation results using the ATLAS b-tagging efficiency in the presence of pile-up are similar to those obtained by using the b-tagging efficiency in the absence of pile-up (the MV1 algorithm).

B. Signal Event Samples

The dominant mechanism for Higgs-pair production is the gluon fusion process at the hadron colliders. Other processes are more than an order of magnitude smaller. Thus, only the gluon fusion production mode is used for the signal process $HH \to b\bar{b}\gamma\gamma$. These samples are generated with `MADGRAPH5_aMC@NLO` at LO [2]. They are showered by `PYTHIA8` to model the parton showering and hadronization. Note that the A14 tune and the `NNPDF2.3LO` PDF [34] set are used together.

The signal event samples are generated with various self-coupling strengths in order to show their characteristics: $-5 \le \lambda_{3H} \le 10$ with $\lambda_{3H} = 1$ being corresponding to the SM Higgs self-coupling strength. And, the expected signal yields are normalized to the cross section computed at next-to-next-to-leading-order (NNLO) accuracy including next-to-next-to-leading-log (NNLL) gluon resummation [18] [3]. In Table II, we show the production cross section times the

[1] It is shown that the rejection factor for pile-up jets could be 1350 with a mean pile-up $\langle\mu\rangle = 200$ [30]. According to ATLAS simulation, only 0% (1.28%) and 0.54% (4.03%) of jets identified as (sub)leading b-jets and reconstructed (sub)leading photons, respectively, originate from pile-up jets.

[2] We use $m_t = 172$ GeV.

[3] For the signal event normalization, we take the cross section computed in the infinite top quark mass approximation [18].

TABLE II. The production cross section times the branching ratio $\sigma \cdot BR(HH \to b\bar{b}\gamma\gamma)$ at the 14 TeV LHC.

λ_{3H}	-4	0	1	2	6	10
$\sigma \cdot BR(HH \to b\bar{b}\gamma\gamma)$ [fb]	1.45	0.25	0.12	0.06	0.48	1.97

branching ratio at the 14 TeV LHC for six selected values of $\lambda_{3H} = -4, 0, 1, 2, 6, 10$. To obtain the production cross section σ for the non-SM values of $\lambda_{3H} \neq 1$, we have used[4]

$$\sigma = \frac{\sigma^{\rm LO}}{\sigma^{\rm LO}_{\rm SM}} \times \sigma^{\rm NNLO+NNLL}_{\rm SM} \, . \tag{7}$$

C. Background Samples

The backgrounds mainly come from the processes with multiple jets and photons. They can mimic the signal-like two photons and two b-jets in the final state. These backgrounds can be categorized into

- Single-Higgs associated backgrounds: $ggH(\gamma\gamma)$, $t\bar{t}H(\gamma\gamma)$, $ZH(\gamma\gamma)$ and $b\bar{b}H(\gamma\gamma)$,
- Non-resonant (continuum) backgrounds: $b\bar{b}\gamma\gamma$, $c\bar{c}\gamma\gamma$, $jj\gamma\gamma$, $b\bar{b}j\gamma$, $c\bar{c}j\gamma$, $b\bar{b}jj$ and $Z(b\bar{b})\gamma\gamma$ events with an additional jet,
- $t\bar{t}$ and $t\bar{t}\gamma$ backgrounds in which at least one of the top quarks decays leptonically.

The information is summarized in Table I.

1. *Single-Higgs associated backgrounds*

The gluon-fusion process $ggH(\gamma\gamma)$ is generated using **POWHEG-BOX** [25] and then the background yield is normalized using the cross section at next-to-next-to-next-leading order (NNNLO) in QCD [18]. The samples for $t\bar{t}H(\gamma\gamma)$, $ZH(\gamma\gamma)$ and $b\bar{b}H(\gamma\gamma)$ are generated using `PYTHIA8` and they are normalized to the cross sections calculated at NLO in QCD [18].

2. *Non-resonant backgrounds*

The non-resonant or continuum background (BG) processes included for the analysis are $b\bar{b}\gamma\gamma$, $c\bar{c}\gamma\gamma$, $jj\gamma\gamma$, $b\bar{b}j\gamma$, $c\bar{c}j\gamma$, $b\bar{b}jj$ and $Z(b\bar{b})\gamma\gamma$. They are all generated with `MADGRAPH5_aMC@NLO` and interfaced with `PYTHIA8` for showering and hadronization, and the `CTEQ6L1` PDF [35] set is taken. Note that these samples are generated inclusively with an additional hard jet to capture the bulk of the NLO corrections. We then avoid the double counting problems in our non-resonant background samples by applying the pre-selection cuts listed in Eq. (6). We have found that the resulting cross sections for the non-resonant backgrounds, presented in Table I, agree with those presented in Ref. [30] within errors of less than 5%.

Among them, as will be shown, the $b\bar{b}\gamma\gamma$ and $b\bar{b}j\gamma$ samples give the dominant BG yields. In the latter, j is faking γ. The sub-dominant BGs come from the $c\bar{c}\gamma\gamma$, $c\bar{c}j\gamma$, and $b\bar{b}jj$ processes with c faking b and/or j faking γ. And the next sub-leading BG is from the $jj\gamma\gamma$ sample. Here, one should be cautious about the $jj\gamma\gamma$ process because it receives contributions not only from the light hard quarks and gluons but also from hard charm quarks. Schematically, one may write [5]

$$\begin{aligned} jj\gamma\gamma &\simeq \sum_{j_h^l, j_h, \mathcal{S}} [1 \oplus j_h^l] \otimes [j_h j_h \gamma\gamma] \otimes [1 \oplus \mathcal{S}] \\ &\simeq \sum_{\{j_h^l\}, \mathcal{S}} \left\{ [1 \oplus j_h^l] \otimes [c_h \bar{c}_h \gamma\gamma] \otimes [1 \oplus \mathcal{S}] \right\} \oplus \left\{ [1 \oplus j_h^l] \otimes [j_h^l j_h^l \gamma\gamma] \otimes [1 \oplus \mathcal{S}] \right\} \, . \end{aligned} \tag{8}$$

---

[4] See also Fig. 2.
[5] For our $jj\gamma\gamma$ analysis, first we have removed c jet from a set of an additional hard jet.

TABLE III. The main fake processes and the corresponding rates in each sample of non-resonant and $t\bar{t}(\gamma)$ backgrounds. We recall that $P_{j\to\gamma} = 5\times10^{-4}$ and $P_{e\to\gamma} = 2\%/5\%$ in the barrel/endcap calorimeter region. For c_s quarks produced during showering in the $jj\gamma\gamma$ sample, we use $P_{c_s\to b} = 1/8$ as in Ref. [30]. Otherwise the P_T and η dependence of $P_{c\to b}$ is fully considered as explained in the text.

Background(BG)	Process	Fake Process	Fake rate
Non-resonant BG	$b\bar{b}\gamma\gamma$	N/A	N/A
	$c\bar{c}\gamma\gamma$	$c\to b,\, \bar{c}\to\bar{b}$	$(P_{c\to b})^2$
	$jj\gamma\gamma$	$c_s\to b,\, \bar{c}_s\to\bar{b}$	$(P_{c_s\to b})^2$
	$b\bar{b}j\gamma$	$j\to\gamma$	5×10^{-4}
	$c\bar{c}j\gamma$	$c\to b,\, \bar{c}\to\bar{b},\, j\to\gamma$	$(P_{c\to b})^2\cdot(5\times10^{-4})$
	$b\bar{b}jj$	$j\to\gamma,\, j\to\gamma$	$(5\times10^{-4})^2$
	$Z(\to b\bar{b})\gamma\gamma$	N/A	N/A
$t\bar{t}$	Leptonic decay	$e\to\gamma,\, e\to\gamma$	$(0.02)^2/0.02\cdot0.05/(0.05)^2$
	Semi-leptonic decay	$e\to\gamma,\, j\to\gamma$	$(0.02)\cdot5\times10^{-4}/(0.05)\cdot5\times10^{-4}$
$t\bar{t}\gamma$	Leptonic decay	$e\to\gamma$	$0.02/0.05$
	Semi-leptonic	$e\to\gamma$	$0.02/0.05$

In the first line, j_h^l [6] in the first bracket denotes the additional light hard jet and $\mathcal{S}$ in the last bracket is for jets generated during the showering process or $\mathcal{S} = j_s^l, j_s^l j_s^l, c_s\bar{c}_s, b_s\bar{b}_s$, etc with the subscript s standing for showering jets. In the second line, we use $j_h j_h \simeq c_h\bar{c}_h \oplus j_h^l j_h^l$ with the subscript h standing for jets from hard scatterings. We definitely see that the first part of Eq. (8) constitutes a part of the $c\bar{c}\gamma\gamma$ sample and should be removed from the $jj\gamma\gamma$ sample to avoid a double counting. After removing it, we find that the process with $\mathcal{S} = c_s\bar{c}_s$ dominates the $jj\gamma\gamma$ BG with c_s faking b. Note that charm quarks should be treated separately from the light quarks since the c-quark fake rate $P_{c\to b}$ is much larger than the light-jet fake rate of $P_{j\to b} = 1/1300$. Incidentally, we recall that $P_{j\to\gamma} = 5\times10^{-4}$. Finally, the $Z(b\bar{b})\gamma\gamma$ sample has the least contribution to the non-resonant backgrounds. In Table III, we are summarizing the main fake processes and rates in each sample of backgrounds.

3. *$t\bar{t}$ and $t\bar{t}\gamma$ backgrounds*

The $t\bar{t}$ background is generated at NLO in QCD using **POWHEG−BOX**, and interfaced to `PYTHIA8` for parton showering and hadronization. And for the PDF set, `CT10` [36] is taken. Since it mimics the signal with an electron in the final state faking a photon, we have required the final state should include at least 1 lepton [7]. And the BG yield is normalized using the cross section calculated with `Top` $++2.0$ program at NNLO in QCD which also includes soft-gluon resummation to NNLL [22]. Here we are taking $m_t = 172.5$ GeV.

A background with a similar size comes from the $t\bar{t}$ production with one photon in the final state. The $t\bar{t}\gamma$ sample is generated at LO in QCD with `MADGRAPH5_aMC@NLO` and interfaced with `PYTHIA8` for showering and hadronization. For $t\bar{t}\gamma$, we are taking the `CTEQ6L1` PDF set and the BG yield is normalized using the cross section calculated in NLO in QCD [23]. Also, as in $t\bar{t}$, we require the final state to contain at least 1 lepton. In Table III, we are summarizing the main fake processes and rates also for the $t\bar{t}$ and $t\bar{t}\gamma$ backgrounds.

D. Event Selections

A sequence of event selections is applied to the signal and background samples. It is clearly listed in Table IV. We follow closely the steps reported in an ATLAS conference report [30]. The goal is to obtain a pair of isolated photons and a pair of isolated b quarks. Both pairs are reconstructed near the Higgs-boson mass. In particular, the cuts $\Delta R_{\gamma\gamma} < 2.0$ and $\Delta R_{bb} < 2.0$ are imposed so as to suppress the main backgrounds which are more populated in the regions of $\Delta R_{\gamma\gamma,bb} > 2.0$, see Fig. 3 [8]. We show the angular separation between photons and that between b jets for

[6] Here, j_h^l denotes a light hard jet originating from light u, d, and s quarks and gluons. Do not confuse it with j_h which is for a hard jet originating not only from the light quarks and gluons but also from c quarks.
[7] Here a lepton means e, μ, or τ.
[8] For larger values of $|\lambda_{3H}|$, the cuts of $\Delta R_{\gamma\gamma,bb} < 2.0$ remove more signal events compared to the SM case, see the upper left frame of Fig. 13 in Appendix A. This leads to the smaller efficiencies as shown in Table V when $\lambda_{3H} = -4$, 6, and 10. We find that the different choices of $\Delta R_{\gamma\gamma,bb}$ cuts hardly improve the signal significance and employ the same cuts taken by the ATLAS group [30].

TABLE IV. Sequence of event selection criteria at the HL-LHC applied in this analysis.

Sequence	Event Selection Criteria at the HL-LHC
1	Di-photon trigger condition, ≥ 2 isolated photons with $P_T > 25$ GeV, $\lvert\eta\rvert < 2.5$
2	≥ 2 isolated photons with $P_T > 30$ GeV, $\lvert\eta\rvert < 1.37$ or $1.52 < \lvert\eta\rvert < 2.37$, $\Delta R_{j\gamma} > 0.4$
3	≥ 2 jets identified as b-jets with leading(sub-leading) $P_T > 40(30)$ GeV, $\lvert\eta\rvert < 2.4$
4	Events are required to contain ≤ 5 jets with $P_T > 30$ GeV within $\lvert\eta\rvert < 2.5$
5	No isolated leptons with $P_T > 25$ GeV, $\lvert\eta\rvert < 2.5$
6	$0.4 < \Delta R_{b\bar{b}} < 2.0$, $0.4 < \Delta R_{\gamma\gamma} < 2.0$
7	$122 < M_{\gamma\gamma}/\text{GeV} < 128$ and $100 < M_{b\bar{b}}/\text{GeV} < 150$
8	$P_T^{\gamma\gamma} > 80$ GeV, $P_T^{b\bar{b}} > 80$ GeV

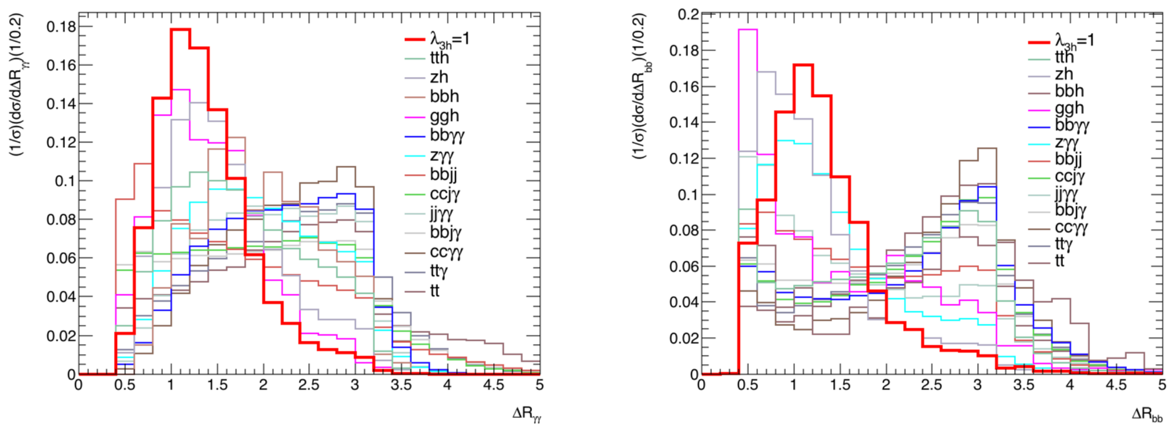

FIG. 3. The $\Delta R_{\gamma\gamma}$ and $\Delta R_{b\bar{b}}$ distributions for the signal with $\lambda_{3H} = 1$ and all the other backgrounds.

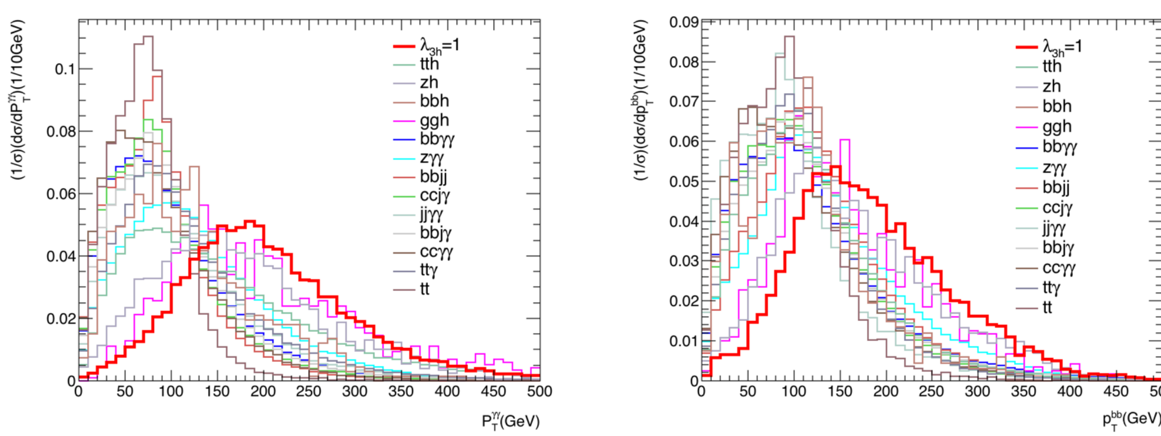

FIG. 4. The transverse momentum distributions $P_T^{\gamma\gamma}$ and $P_T^{b\bar{b}}$ for the signal with $\lambda_{3H} = 1$ and all the other backgrounds.

all the backgrounds and the signal with $\lambda_{3H} = 1$ in the left and right frame of Fig. 3, respectively. It is clear that the majority of the signal and a very few backgrounds lie in the region $\Delta R_{\gamma\gamma} < 2$ and $\Delta R_{bb} < 2$. In Fig. 4, we show the transverse momentum distributions $P_T^{\gamma\gamma}$ and $P_T^{b\bar{b}}$ for the signal with $\lambda_{3H} = 1$ and all the backgrounds. We observe the signal tends to have larger transverse momentum. Distributions of $\Delta R_{\gamma\gamma}$ and $P_T^{\gamma\gamma}$ with other values of λ_{3H} can be found in Appendix A where we also show the $\Delta R_{\gamma j}$ and $M_{\gamma\gamma bb}$ distributions. The details of cuts are summarized in Table IV.

All events passing the above selection criteria are classified into two categories, depending on the pseudorapidities of the photons. If both photons appear in the barrel region ($|\eta| < 1.37$) the event is labeled as "barrel-barrel", otherwise it is labeled as "other".

E. Cut Flows and Efficiencies

We follow closely the steps used in the ATLAS conference note [30]. We compare the cut flow of our current analysis with ATLAS results for the $\lambda_{3H} = 1$ case, and they agree with each other within about 5–15%. We show in Table V the efficiencies and event yields for Higgs-pair production in the channel $HH \to b\bar{b}\gamma\gamma$ at the HL-LHC with an integrated luminosity of 3000 fb^{-1} for various values of $\lambda_{3H} = -4, 0, 1, 2, 6, 10$. In the last row, "other/barrel ratio" is the ratio of events for the two photon candidates falling in the "other" region to those in the "barrel-barrel" region, after applying all the event selection cuts. The overall other/barrel ratios are all similar.

The overall signal efficiency has its peak value of 3.79 % at $\lambda_{3H} = 2$ and it decreases when λ_{3H} deviates from 2. We observe that the overall efficiency drops quickly when λ_{3H} moves to a larger value and becomes smaller than 1 % when $\lambda_{3H} \gtrsim 4$. While when λ_{3H} becomes smaller and starts to take on negative values, it decreases to 3.17 % at the SM value of $\lambda_{3H} = 1$ and reaches 1.77 % at $\lambda_{3H} = -4$. This is because of the strong destructive (constructive) interference between the triangle and box diagrams for the positive (negative) values of λ_{3H} and the enhancement of kinematical features of the triangle diagram for $|\lambda_{3H}| > 1$. Thus, these two effects are combined to give strong dependence of the $\Delta R_{\gamma\gamma,bb}$ distributions on λ_{3H}, and therefore leading to the strong dependence of the signal efficiency on λ_{3H}. On the other hand, the number of signal events, which is given by the product of the cross section, signal efficiency, and luminosity of 3000 fb^{-1}, is only 7 at $\lambda_{3H} = 2$ but it becomes 11 at the SM value of $\lambda_{3H} = 1$. Note that one may have the same number of signal events also at $\lambda_{3H} = 6$.

The cut flow tables of all the backgrounds in terms of efficiencies at the HL-LHC are presented in Appendix B.

F. Analysis and Results

Here we show the main results of our analysis in Table VI – the resultant signal rates for various λ_{3H} against all the backgrounds. The last column is for the number of generated events in each sample. The statistical uncertainties originating from the limited number of generated events are estimated by dividing each of the background and signal samples into roughly $O(10)$ subsamples. The fluctuations among the subsamples are then taken as the uncertainty of the sample. We have made detailed comparisons with the results from ATLAS [30]. In general we agree, except for ggH and $t\bar{t}$. In the ggH sample, we figure out that about half of the disagreement is caused by the differences in b-tagging algorithm and detector simulations. While, for the $t\bar{t}$ sample, our estimation is made based on the **Delphes3** algorithm for electron reconstruction and identification which is about 20 times more efficient than that taken by ATLAS.

More precisely, in the ggH sample, our number of the ggH background is 6.60 which is 2.4 times larger than the ATLAS number of 2.74 [30]. By noting that the ggH sample is dominated by b quarks from showering processes, we find a part of the difference can be attributed to different b-tagging algorithm taken in our work: ours is from [32] while, in the ATLAS paper, the algorithm from [37] is used. If we use the same algorithm taken in the ATLAS paper, we find the number of background reduces to about 5 which is still a bit above the ATLAS number 2.74. We also find another reason in the detector simulations but, again, it is not enough to fully explain the difference. Indeed, the similar observation has been recently made by the authors of Ref. [13]. When they used the same selection cuts as ATLAS, the result was also larger than the ATLAS result, but consistent with ours.

We note that the kinematic distributions for the signal with different λ_{3H} would not be very different, as seen by the ratio (O/B) in the last of Table VI, which are more or less the same for different λ_{3H}. On the other hand, the ratio (O/B) for the backgrounds, on average, is larger than the signal, which means the backgrounds are in general more forward. We further note that the combined significance obtained by splitting events into two categories of barrel-barrel and other is improved by 3 % over the total one when $\lambda_{3H} = 1$. For our analysis, we use the combined significance.

The most dominant one in the single-Higgs associated backgrounds is $t\bar{t}H$ followed by ggH. The single-Higgs associated processes contribute about 23 events to the total background. Meanwhile the dominant ones in non-resonant backgrounds are $b\bar{b}\gamma\gamma$ and $b\bar{b}j\gamma$ with each of it contributing 19 events to the total background. A similar size of background comes from combined $c\bar{c}\gamma\gamma \oplus c\bar{c}j\gamma \oplus jj\gamma\gamma$, in which either hard or showering c quarks are faking b

TABLE V. Efficiencies (%) and event yields (#): the signal cut flows for Higgs-pair production at LHC 14 TeV with an integrated luminosity of 3000 fb^{-1} for λ_{3H}=-4,0,1,2,6,10.

λ_{3H}	-4		0		1		2		6		10	
Cross section (fb)	1.45		0.25		0.12		0.06		0.48		1.97	
Cuts	Eff.%	No.#	%	No.#	%	No.#	%	#	%	#	%	#
1. diphoton trigger	23.15	1007	25.63	192	27.47	99	28.94	52	20.50	295	21.01	1242
2. ≥ 2 isolated photons	20.79	904	23.33	175	25.21	91	26.73	48	17.82	257	18.38	1086
3-1. jet candidates	14.58	634	17.10	128	19.07	69	20.85	38	11.62	167	12.14	717
3-2 ≥ 2 two b-jet	4.61	200	5.65	42	6.46	23	7.26	13	3.34	48	3.55	210
4. no. of jets ≤ 5	4.47	194	5.43	41	6.23	22	6.97	13	3.26	47	3.45	204
5. lepton veto	4.41	192	5.36	40	6.15	22	6.88	12	3.22	46	3.41	202
6. $\Delta R_{\gamma\gamma,bb}$ cut	2.72	118	4.00	30	4.98	18	5.87	11	1.19	17	1.49	88
7-1. Higgs mass window $M_{\gamma\gamma}$	2.65	115	3.88	29	4.82	17	5.64	10	1.15	17	1.46	86
7-2. Higgs mass window M_{bb}	1.80	78	2.62	20	3.20	12	3.82	7	0.78	11	0.99	59
8. $p_{T_{\gamma\gamma}}, p_{T_{bb}}$ cuts	1.77	77	2.60	20	3.17	11	3.79	7	0.77	11	0.97	57
other/barrel ratio	35.27 %		36.08%		33.89%		32.66%		39.47%		37.01%	

TABLE VI. HL-LHC yields: Expected number of signal and background events at the HL-LHC assuming 3000 fb^{-1}. We separate the backgrounds into three categories (See text). The significance for $\lambda_{3H} = 1$ (SM) is also shown, see Eq. (9). The combined significance is given by the square root of the sum of the squares of the "barrel-barrel" and "other" significances.

Expected yields (3000 fb^{-1}) Samples	Total	Barrel-barrel	Other (End-cap)	Ratio (O/B)	# of Gen. Events
$H(b\bar{b})\,H(\gamma\gamma)$, $\lambda_{3H} = -4$	77.14 ± 0.94	57.03 ± 0.75	20.11 ± 0.34	0.35 ± 0.01	3×10^5
$H(b\bar{b})\,H(\gamma\gamma)$, $\lambda_{3H} = 0$	19.50 ± 0.20	14.33 ± 0.16	5.17 ± 0.13	0.36 ± 0.01	3×10^5
$H(b\bar{b})\,H(\gamma\gamma)$, $\lambda_{3H} = 1$	11.42 ± 0.082	8.53 ± 0.092	2.89 ± 0.048	0.34 ± 0.01	3×10^5
$H(b\bar{b})\,H(\gamma\gamma)$, $\lambda_{3H} = 2$	6.82 ± 0.05	5.14 ± 0.04	1.68 ± 0.03	0.33 ± 0.01	3×10^5
$H(b\bar{b})\,H(\gamma\gamma)$, $\lambda_{3H} = 6$	11.03 ± 0.21	7.91 ± 0.23	3.12 ± 0.10	0.39 ± 0.02	3×10^5
$H(b\bar{b})\,H(\gamma\gamma)$, $\lambda_{3H} = 10$	57.46 ± 1.01	41.94 ± 0.60	15.52 ± 0.62	0.37 ± 0.02	3×10^5
$gg\,H(\gamma\gamma)$	6.60 ± 0.69	4.50 ± 0.71	2.10 ± 0.30	0.47 ± 0.10	6×10^6
$t\,\bar{t}\,H(\gamma\gamma)$	13.21 ± 0.23	9.82 ± 0.19	3.39 ± 0.17	0.35 ± 0.02	10^6
$Z\,H(\gamma\gamma)$	3.62 ± 0.16	2.44 ± 0.16	1.18 ± 0.08	0.48 ± 0.05	10^6
$b\,\bar{b}\,H(\gamma\gamma)$	0.15 ± 0.024	0.11 ± 0.027	0.04 ± 0.014	0.40 ± 0.16	10^6
$b\,\bar{b}\,\gamma\,\gamma$	18.86 ± 0.9	11.15 ± 0.7	7.71 ± 0.5	0.69 ± 0.06	1.1×10^7
$c\,\bar{c}\,\gamma\,\gamma$	7.53 ± 1.06	4.79 ± 1.10	2.74 ± 0.81	0.57 ± 0.21	10^7
$j\,j\,\gamma\,\gamma$	3.34 ± 0.46	1.59 ± 0.31	1.75 ± 0.32	1.10 ± 0.29	10^7
$b\,\bar{b}\,j\,\gamma$	18.77 ± 1.00	10.40 ± 0.83	8.37 ± 0.63	0.80 ± 0.09	10^7
$c\,\bar{c}\,j\,\gamma$	5.52 ± 1.4	3.94 ± 1.0	1.58 ± 0.6	0.40 ± 0.18	10^7
$b\,\bar{b}\,j\,j$	5.54 ± 0.5	3.81 ± 0.3	1.73 ± 0.2	0.45 ± 0.06	5×10^6
$Z(b\bar{b})\,\gamma\gamma$	0.90 ± 0.03	0.54 ± 0.02	0.36 ± 0.02	0.67 ± 0.04	10^7
$t\,\bar{t}$ (≥ 1 leptons)	4.98 ± 0.23	3.04 ± 0.12	1.94 ± 0.21	0.64 ± 0.07	10^7
$t\,\bar{t}\,\gamma$ (≥ 1 leptons)	3.61 ± 0.21	2.29 ± 0.15	1.32 ± 0.15	0.58 ± 0.08	10^7
Total Background	92.63 ± 2.5	58.42 ± 2.0	34.21 ± 1.4	0.59 ± 0.03	
Significance Z	1.163	1.090	0.487		
Combined significance		1.194			

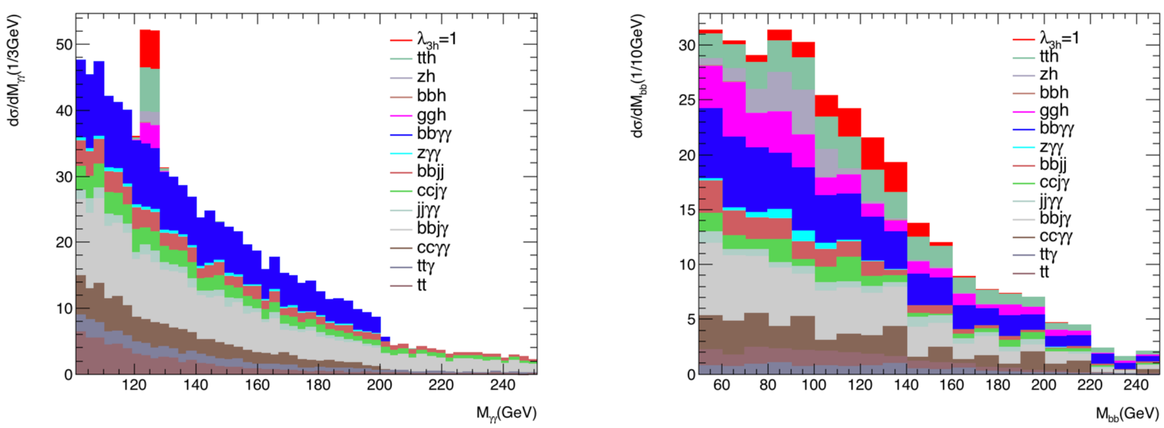

FIG. 5. The $M_{\gamma\gamma}$ (upper) and $M_{b\bar{b}}$ (lower) distributions for the signal on top of the backgrounds at the HL-LHC.

jets basically. Among the non-resonant backgrounds, $b\bar{b}jj$ contributes the least. Including $t\bar{t}$ and $t\bar{t}\gamma$ in which one or two electrons are faking photons, we note that more than one half of the total background is due to fakes.

In Fig. 5, we show the resultant invariant-mass distributions of the two photon (upper) and two b (lower) candidates for the signal on top of all the backgrounds. We have applied all the selection cuts except for the cut on $M_{\gamma\gamma}$ ($M_{b\bar{b}}$) in the upper (lower) frame. The photon peak $M_{\gamma\gamma} \sim 125$ GeV is very clear while that of $M_{b\bar{b}} \sim 125$ GeV is rather

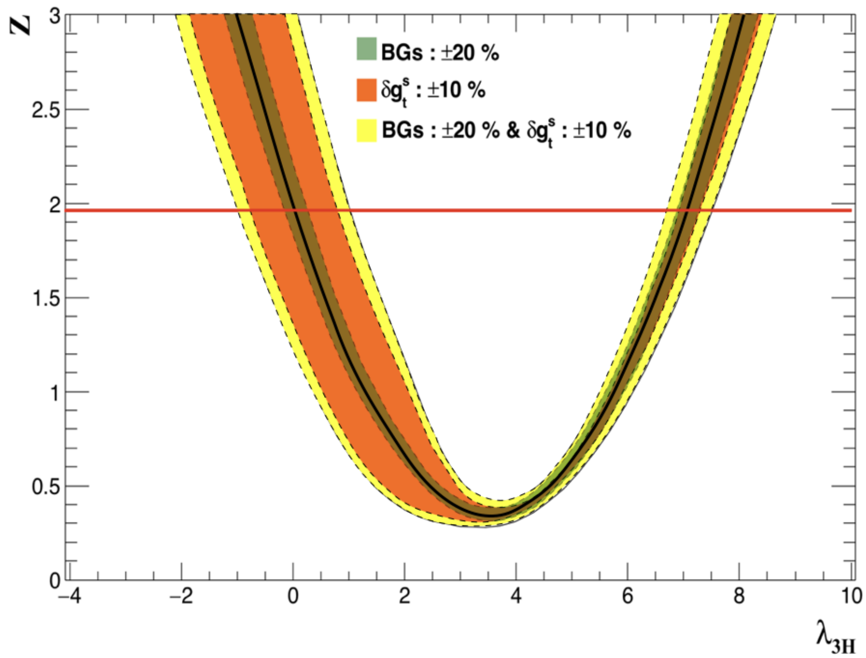

FIG. 6. **HL-LHC**: Significance of the signal over the background versus λ_{3H}. The orange and green bands represents the impact of the uncertainties associated with the top-Yukawa coupling and the estimation of backgrounds, respectively, and the yellow one the impact of both of the uncertainties. The black solid line is for the case when $g_t^S = 1$ and $b = 92.63$, see Table VI.

broad, due to the b-jet resolution.

In Fig. 6, we show the significance defined by

$$Z = \sqrt{2 \cdot [((s+b) \cdot \ln(1+s/b) - s)]} \tag{9}$$

where s and b represent the numbers of signal and background events, respectively. The central curve is for the case when the top-Yukawa coupling takes on the SM value of $g_t^S = 1$ and $b = 92.63$, see Table VI. The orange and green bands have been obtained by varying the top-Yukawa coupling by 10 % [9] ($|\delta g_t^S| \leq 0.1$) and the total background yield by 20 % ($|\delta b/b| \leq 0.2$), respectively. The yellow band has been obtained by considering both of the uncertainties simultaneously. The uncertainty associated with the estimation of backgrounds may arise from pile-up, the photon and b-tagging efficiencies, several fake rates, the choices of renormalization and factorizations scales and PDF, etc. We note that the δg_t^S effect becomes larger when λ_{3H} decreases from 3.5. For $\lambda_{3H} \gtrsim 3.5$, the δb effect could be comparably important. Given all the uncertainties can be minimized and the top-Yukawa at the SM value, the 95% CL sensitivity region for λ_{3H} is $0 < \lambda_{3H} < 7.1$. However, given the worst uncertainties with $\delta g_t^S = \pm 0.1$ and $\delta b/b = \pm 0.2$, the sensitivity range widens to $-1.0 < \lambda_{3H} < 7.6$. We note that the lower boundary of the 95% CL region of λ_{3H} is sensitive to the top-Yukawa g_t^S while the impact of the uncertainty associated with the estimation of backgrounds turns out minor upon the 20 % variation over the total background.

Finally, we show in Fig. 7 the luminosity required to achieve 95% CL sensitivity versus λ_{3H}. We observe that the SM value of $\lambda_{3H} = 1$ can only be established with about 8.5 ab^{-1} luminosity. Note that the required luminosity peaks at $\lambda_{3H} \simeq 3.5$ while the $gg \to HH$ production takes its smallest value at $\lambda_{3H} \simeq 2.5$, see Fig. 1. This is because of the strong dependence of the signal efficiency on λ_{3H} induced by the substantial interference between the triangle and box diagrams together with, especially for $|\lambda_{3H}| > 1$, the enhancement of kinematical features of the triangle diagram or the smaller Higgs-pair invariant mass of $M_{\gamma\gamma bb}$, the wider angular separations of $\Delta R_{\gamma\gamma,bb}$, and the smaller transverse momenta of $P_T^{\gamma\gamma,bb}$.

---

[9] In our work, we also take account of the effect of the 10 % uncertainty of the top-Yukawa coupling on the ggH and $t\bar{t}H$ backgrounds while neglecting its effect on the Higgs decay mode into two photons since it is dominated by the W loops. Incidentally, we have taken the SM values for the Higgs couplings to b quarks and W bosons for $H \to \gamma\gamma$.

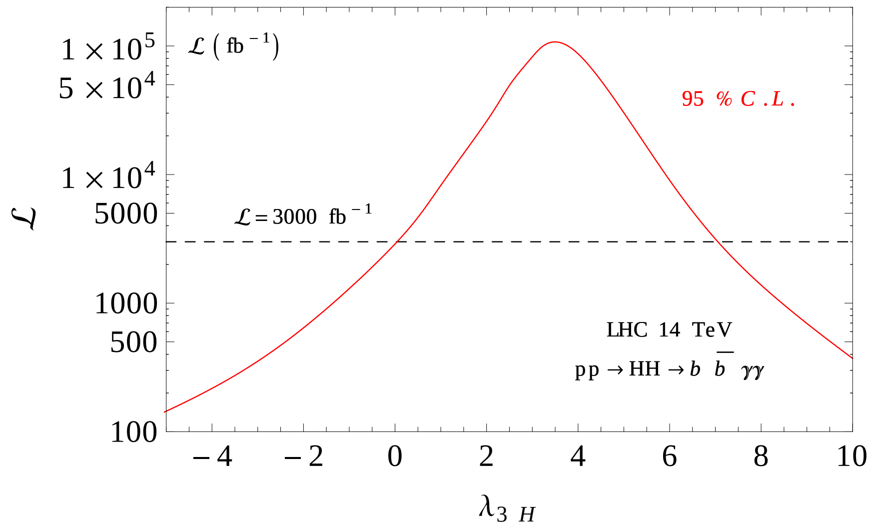

FIG. 7. **HL-LHC**: Required luminosity for 95% CL sensitivity at the 14 TeV HL-LHC versus λ_{3H}. Here we assume that the top-Yukawa coupling takes the SM value.

IV. SIMULATIONS, EVENT SELECTIONS, AND ANALYSIS AT THE HL-100 TEV COLLIDER

In this section, through the $HH \to b\bar{b}\gamma\gamma$ channel, we estimate how well one can measure the λ_{3H} coupling at a 100 TeV hadron collider assuming a nominal luminosity of 3 ab^{-1} or at the HL-100 TeV hadron collider. We basically follow the procedures that we took in the last section for the 14 TeV HL-LHC case, though some selection cuts may be changed because of the much higher center-of-mass energy. We have taken a crude estimate projected from the current LHC detectors for the P_T and η coverage for jets, leptons, and photons without any specific detector designs available for the 100 TeV hadron collider.

A. Parton-level event generations and detector simulations

The same signal and backgrounds are considered as in the 14 TeV case. The Monte Carlo generators, the cross sections, and the orders of QCD calculation are shown in Table VII. Note that, for some backgrounds, the orders in QCD are different compared to the 14 TeV case. Otherwise, the calculational methods taken for the signal and background samples are essentially the same as those what we employed for the HL-LHC.

On the other hand, pre-selection cuts, detector energy resolutions, and tagging efficiencies and fake rates may undergo significant changes because of different designs and projected performance of the detectors in the future. Below, we describe in detail what we use in our analysis.

- Pre-selection cuts, which are imposed in order to avoid any divergence in the parton- level calculations, are modified as follows to match the wider η coverage of future particle detectors:

$$\begin{aligned} P_{T_j} > 20 \ \text{GeV},\ P_{T_b} > 20 \ \text{GeV},\ P_{T_\gamma} > 25 \ \text{GeV},\ P_{T_l} > 10 \ \text{GeV}, \\ |\eta_j| < 6,\ |\eta_\gamma| < 6,\ |\eta_l| < 6,\ \Delta R_{jj,ll,\gamma\gamma,\gamma j,jl,\gamma l} > 0.4, \\ M_{jj} > 25 \text{ GeV},\ M_{bb} > 45 \text{ GeV},\ 60 < M_{\gamma\gamma} < 200 \text{ GeV}. \end{aligned}$$

- Fast detector simulation and analysis at the HL-100 TeV hadron collider are performed using **`Delphes3`** [31] with the FCChh template. For the energy resolution of the detector, we have chosen the "Medium" detector performance for ECAL and HCAL [20] [10] because we could get the best significance for this choice. In the "Medium" performance scenario, the ECAL energy resolution is given by

$$\Delta E/E|_{\text{ECAL}} = \sqrt{0.01^2 + 0.1^2 \,\text{GeV}/E}$$

---

[10] In Ref. [20], three scenarios of ECAL and HCAL performance are considered: "Low", "Medium", and "High".

TABLE VII. The same as in Table I but for a 100 TeV hadron collider. In the row for $b\bar{b}H(\to\gamma\gamma)$, 5FS stands for the 5-flavor scheme. Note that, except the $ggH(\to\gamma\gamma)$ background which is generated at NLO, all the signal and backgrounds are generated at LO and normalized to the cross sections computed at the accuracy denoted in 'Order in QCD'.

Signal					
Signal process		Generator/Parton Shower	$\sigma\cdot BR$ [fb]	Order in QCD	PDF used
$gg\to HH\to b\bar{b}\gamma\gamma$ [20]		`MG5_aMC@NLO/PYTHIA8`	4.62	NNLO +NNLL	NNPDF2.3LO
Backgrounds					
Background(BG)	Process	Generator/Parton Shower	$\sigma\cdot BR$ [fb]	Order in QCD	PDF used
Single-Higgs associated BG	$ggH(\to\gamma\gamma)$ [20]	`POWHEG - BOX/PYTHIA8`	1.82×10^3	NNNLO	`CT10`
	$t\bar{t}H(\to\gamma\gamma)$ [20]	`PYTHIA8/PYTHIA8`	7.29×10^1	NLO	
	$ZH(\to\gamma\gamma)$ [20]	`PYTHIA8/PYTHIA8`	2.54×10^1	NNLO	
	$b\bar{b}H(\to\gamma\gamma)$ [38]	`PYTHIA8/PYTHIA8`	1.96×10^1	NNLO(5FS)	
Non-resonant BG	$b\bar{b}\gamma\gamma$	`MG5_aMC@NLO/PYTHIA8`	4.93×10^3	LO	`CTEQ6L1`
	$c\bar{c}\gamma\gamma$	`MG5_aMC@NLO/PYTHIA8`	4.54×10^4	LO	
	$jj\gamma\gamma$	`MG5_aMC@NLO/PYTHIA8`	5.38×10^5	LO	
	$b\bar{b}j\gamma$	`MG5_aMC@NLO/PYTHIA8`	1.44×10^7	LO	
	$c\bar{c}j\gamma$	`MG5_aMC@NLO/PYTHIA8`	4.20×10^7	LO	
	$b\bar{b}jj$	`MG5_aMC@NLO/PYTHIA8`	1.60×10^{10}	LO	
	$Z(\to b\bar{b})\gamma\gamma$	`MG5_aMC@NLO/PYTHIA8`	9.53×10^1	LO	
$t\bar{t}$ and $t\bar{t}\gamma$ BG [20] (≥1 lepton)	$t\bar{t}$	`MG5_aMC@NLO/PYTHIA8`	1.76×10^7	NLO	`CT10`
	$t\bar{t}\gamma$	`MG5_aMC@NLO/PYTHIA8`	4.18×10^4	NLO	`CTEQ6L1`

and the HCAL energy resolution by

$$\Delta E/E|_{\rm HCAL}=\begin{cases}\sqrt{0.03^2+0.5^2\,{\rm GeV}/E} & \text{for } \ |\eta|\leq4\,,\\ \sqrt{0.05^2+1.0^2\,{\rm GeV}/E} & \text{for } \ 4<|\eta|\leq6\,.\end{cases}$$

Further we set the magnetic field 6 T and the jet energy scale of 1.135 is taken to get the correct peak position at M_H in the invariant mass distribution of the b-quark pair in the signal process.

- For the b-jet tagging efficiency and related jet fake rates, we are taking $\epsilon_b=75$ %, $P_{c\to b}=10$ %, and $P_{j\to b}=1$ % [20].
- For the photon efficiency and jet fake rate, we are taking: $\epsilon_\gamma=95\,\%\,(|\eta_\gamma|\leq1.5)$, $90\,\%$ $(1.5<|\eta_\gamma|\leq4)$, $80\,\%$ $(4<|\eta_\gamma|\leq6)$, and $P_{j\to\gamma}=1.35\times10^{-3}$ [20]. For the $e\to\gamma$ fake rate, with a separation between the barrel and endcap regions at $|\eta|=2$, we take $P_{e\to\gamma}=2\,\%\,(5\,\%)$ in the barrel (endcap) region as a reference [30] .

B. Signal Event Samples

The signal event samples are generated in exactly the same way as in the HL-LHC case. We show the production cross section times the branching ratio at the 100 TeV pp collider for six selected values of $\lambda_{3H}=-4,0,1,2,6,10$ in Table VIII.

TABLE VIII. Production cross section times the branching ratio $\sigma\cdot BR(HH\to b\bar{b}\gamma\gamma)$ at the 100 TeV pp collider.

λ_{3H}	-4	0	1	2	6	10
$\sigma\cdot BR(HH\to b\bar{b}\gamma\gamma)$ [fb]	46.97	8.99	4.62	2.32	13.61	57.78

C. Background Samples

As in the HL-LHC case, we categorize the backgrounds into single-Higgs associated backgrounds, non-resonant backgrounds, and $t\bar{t}$ and $t\bar{t}\gamma$ backgrounds. The information is summarized in Table VII. Note that the $t\bar{t}$ sample is generated with MADGRAPH5_aMC@NLO, and for showering, hadronization and decays of unstable particles only PYTHIA8 is used [11]. Otherwise, the descriptions of the backgrounds are the same as in the HL-LHC case.

The cross sections increase as we move from 14 TeV to 100 TeV. The signal cross section increases by a factor of about 40. The cross section for the single-Higgs associated backgrounds increases by a factor of about 15 except $t\bar{t}H(\to\gamma\gamma)$: the increment factor for the $t\bar{t}H(\to\gamma\gamma)$ process is about 50. The cross section for the $Z(\to b\bar{b})\gamma\gamma$ process increases by a factor of about 20 while the increment factor of the other non-resonant backgrounds is about 40. The cross sections for the $t\bar{t}$ related backgrounds increase by about 30 times. As we will show, the non-resonant backgrounds constitutes more than 75 % of the total backgrounds. Roughly, the cross sections for the signal and dominant background processes increase by a factor of about 40. Finally, in Table IX, we summarize the faking rates of non-resonant and $t\bar{t}$-related backgrounds which we use for the HL-100 TeV collider.

TABLE IX. The main fake processes and the corresponding faking rates in each sample of non-resonant and $t\bar{t}(\gamma)$ backgrounds. We recall that $P_{j\to\gamma} = 1.35\times10^{-3}$, $P_{c\to b} = P_{c_s\to b} = 0.1$ [20] and $P_{e\to\gamma} = 2\%/5\%$ in the barrel/endcap calorimeter region.

Background(BG)	Process	Fake Process	Fake rate
Non-resonant BG	$b\bar{b}\gamma\gamma$	N/A	N/A
	$c\bar{c}\gamma\gamma$	$c\to b,\ \bar{c}\to\bar{b}$	$(0.1)^2$
	$jj\gamma\gamma$	$c_s\to b,\ \bar{c}_s\to\bar{b}$	$(0.1)^2$
	$b\bar{b}j\gamma$	$j\to\gamma$	1.35×10^{-3}
	$c\bar{c}j\gamma$	$c\to b,\ \bar{c}\to\bar{b},\ j\to\gamma$	$(0.1)^2\cdot(1.35\times10^{-3})$
	$b\bar{b}jj$	$j\to\gamma,\ j\to\gamma$	$(1.35\times10^{-3})^2$
	$Z(\to b\bar{b})\gamma\gamma$	N/A	N/A
$t\bar{t}$	Leptonic decay	$e\to\gamma,\ e\to\gamma$	$(0.02)^2/0.02\cdot0.05/(0.05)^2$
	Semi-leptonic decay	$e\to\gamma,\ j\to\gamma$	$(0.02)\cdot1.35\times10^{-3}/(0.05)\cdot1.35\times10^{-3}$
$t\bar{t}\gamma$	Leptonic decay	$e\to\gamma$	0.02/0.05
	Semi-leptonic	$e\to\gamma$	0.02/0.05

D. Event Selections

A sequence of event selections is applied to the signal and background samples, see Table X. We basically follow our HL-LHC analysis but using more relaxed ΔR condition to inclusively cover the broad range of λ_{3H} still allowed after the HL-LHC era. Also considered are the wider $|\eta|$ coverage at 100 TeV and the more energetic jets and photons.

The distributions in $\Delta R_{\gamma\gamma}$, ΔR_{bb}, $P_T^{\gamma\gamma}$, P_T^{bb}, $\Delta R_{\gamma b}$, and $M_{\gamma\gamma bb}$ are very similar to the case of HL-LHC. We collect some of them in appendix A in order not to interrupt smooth reading of the main text.

E. Cut Flows and Efficiencies

We closely follow the procedures that we employed for the HL-LHC. We show in Table XI the efficiencies and event yields for Higgs-pair production in the channel $HH\to b\bar{b}\gamma\gamma$ with $\lambda_{3H} = -4, 0, 1, 2, 6, 10$ and an integrated luminosity of 3000 fb^{-1} at the 100 TeV collider.

The overall signal efficiency has its peak value of 8.01 % at $\lambda_{3H} = 2$ and its behavior is similar to that at 14 TeV with ~ 2 % when $\lambda_{3H} \gtrsim 4$, 6.79 % at the SM value of $\lambda_{3H} = 1$, and 3.98 % at $\lambda_{3H} = -4$. On the other hand, the number of signal event is 557 at $\lambda_{3H} = 2$ and it becomes 941 at the SM value of $\lambda_{3H} = 1$. Note that one may have a similar number of signal events at $\lambda_{3H} = 6$.

The cut flow table of all the backgrounds in terms of efficiencies at the HL-100 TeV hadron collider is presented in Appendix B.

[11] Note PYTHIA6 is used for the $ggH(\to\gamma\gamma)$ process at the HL-LHC.

TABLE X. Sequence of event selection criteria at the HL-100 TeV hadron collider applied in this analysis.

Sequence	Event Selection Criteria at the HL-100 TeV hadron collider
1	Di-photon trigger condition, ≥ 2 isolated photons with $P_T > 30$ GeV, $\lvert\eta\rvert < 5$
2	≥ 2 isolated photons with $P_T > 40$ GeV, $\lvert\eta\rvert < 3$, $\Delta R_{j\gamma} > 0.4$
3	≥ 2 jets identified as b-jets with leading(sub-leading) $P_T > 50(40)$ GeV, $\lvert\eta\rvert < 3$
4	Events are required to contain ≤ 5 jets with $P_T > 40$ GeV within $\lvert\eta\rvert < 5$
5	No isolated leptons with $P_T > 40$ GeV, $\lvert\eta\rvert < 3$
6	$0.4 < \Delta R_{b\bar{b}} < 3.0$, $0.4 < \Delta R_{\gamma\gamma} < 3.0$
7	$122.5 < M_{\gamma\gamma}/\text{GeV} < 127.5$ and $90 < M_{b\bar{b}}/\text{GeV} < 150$
8	$P_T^{\gamma\gamma} > 100$ GeV, $P_T^{b\bar{b}} > 100$ GeV

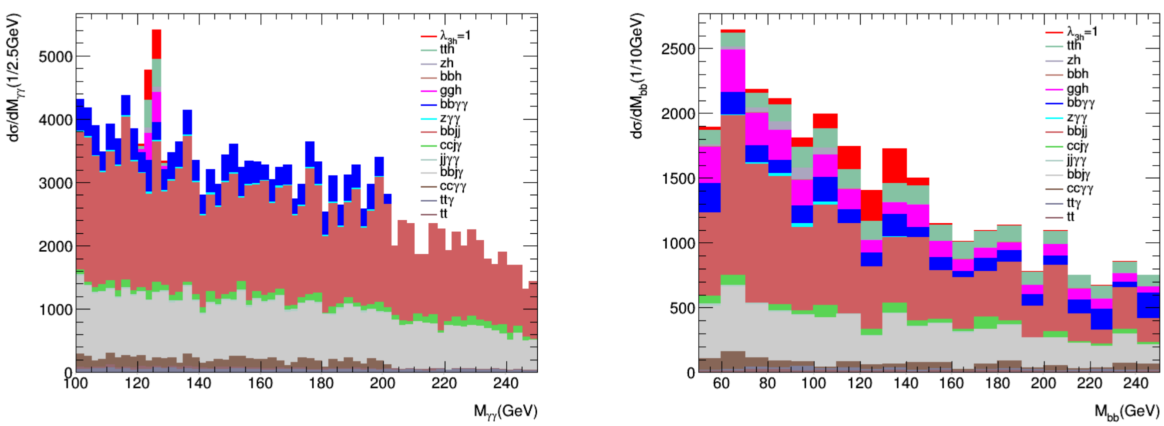

FIG. 8. The $M_{\gamma\gamma}$ (upper) and $M_{b\bar{b}}$ (lower) distributions for the signal on top of all the backgrounds at the HL-100 TeV hadron collider.

F. Analysis and Results

Here we show the main results of the analysis for the 100 TeV hadron collider, see Table XII. Among the single-Higgs associated backgrounds, the major ones come from ggH and $t\bar{t}H$, comprising about 20 % of the total background. Meanwhile the dominant ones in non-resonant backgrounds are $b\bar{b}jj$ followed $b\bar{b}j\gamma$ which make up about 60 % of the total background. Including other backgrounds, we note that 70 % of the total background is due to fakes. Being contrary to the HL-LHC case, the combined significance achieved is much higher: $Z = 9.981$ at the SM value of $\lambda_{3H} = 1$, which is mainly because of much higher signal event rates though the signal to background ratios are similar at HL-LHC and HL-100 TeV collider.

In Fig. 8, we show the resultant invariant-mass distributions of the two photon (upper) and two b (lower) candidates for the signal on top of all the backgrounds at the HL-100 TeV collider, as similar to HL-LHC in Fig. 5. We observe the similar behavior as in the HL-LHC case.

Since the achieved significance is high enough, we try to estimate how well one can measure the λ_{3H} coupling at the HL-100 TeV hadron collider. In the left frame of Fig. 9, we show the number of signal events N as a function of λ_{3H}. To obtain the curve we assume the luminosity of 3 ab^{-1} and take into account the λ_{3H}-dependent overall signal efficiencies, see Table XI. One may find the values of N for some representative choices of λ_{3H} in Table XII. On the other hand, the solid horizontal line shows the number of signal events s, as an example, when the input value of λ_{3H} or λ_{3H}^{in} takes the SM value of 1. The dotted lines delimit the 1-σ region considering the statistical error of $\Delta s = \sqrt{s+b}$ with $b = 9147.63$. For this purpose, we generate another pseudo dataset for the signal. By locating the points where the N curve and the horizontal lines meet, one can obtain the two center values of output λ_{3H} and the corresponding two regions of 1-σ error. Note that, usually, there is a two-fold ambiguity in this approach. By repeating this procedure for different input values of λ_{3H}, we can obtain the center output λ_{3H} values together with

TABLE XI. The same as in Table V but at the 100 TeV hadron collider with an integrated luminosity of 3 ab^{-1}.

λ_{3H}	-4		0		1		2		6		10	
Cross section (fb)	46.97		8.99		4.62		2.32		13.61		57.78	
Cuts	Eff.%	No.#	%	No.#	%	No.#	%	#	%	#	%	#
1. diphoton trigger	56.06	78988	57.78	15582	58.99	8176	60.00	4176	53.44	21818	53.82	93293
2. ≥ 2 isolated photons	36.31	51158	39.21	10575	41.29	5722	43.40	3021	32.39	13225	32.94	57105
3-1. jet candidates	29.07	40965	32.77	8838	35.36	4901	37.94	2641	23.87	9746	24.74	42881
3-2 ≥ 2 two b-jet	9.57	13492	11.41	3076	12.75	1767	14.18	987	7.31	2986	7.65	13252
4. no. of jets ≤ 5	9.03	12724	10.60	2860	11.79	1634	13.04	907	6.99	2856	7.29	12638
5. lepton veto	9.03	12724	10.60	2860	11.79	1634	13.04	907	6.99	2856	7.29	12637
6. $\Delta R_{\gamma\gamma,bb}$ cut	8.32	11730	10.08	2718	11.34	1572	12.57	875	5.92	2419	6.39	11023
7-1. Higgs mass window $M_{\gamma\gamma}$	7.78	10968	9.35	2523	10.51	1456	11.57	805	5.55	2268	5.97	10341
7-2. Higgs mass window M_{bb}	6.14	8650	7.32	1974	8.23	1140	9.08	632	4.48	1830	4.77	8264
8. $p_{T_{\gamma\gamma}}, p_{T_{bb}}$ cuts	3.98	5604	5.61	1514	6.79	941	8.01	557	1.84	753	2.21	3838
other/barrel ratio	31.64%		30.14%		30.05%		29.18%		33.03%		31.26%	

TABLE XII. The same as in Table VI but at the HL-100 TeV hadron collider with an integrated luminosity of 3 ab^{-1}.

Expected yields (3000 fb^{-1}) Samples	Total	Barrel-barrel	Other (End-cap)	Ratio (O/B)	# of Gen. Events
$H(b\bar{b})\,H(\gamma\gamma)$, $\lambda_{3H}=-4$	5604.46 ± 63.36	4257.36 ± 57.90	1347.10 ± 23.22	0.32 ± 0.007	3×10^5
$H(b\bar{b})\,H(\gamma\gamma)$, $\lambda_{3H}=0$	1513.56 ± 14.81	1163.04 ± 14.09	350.52 ± 3.57	0.30 ± 0.005	3×10^5
$H(b\bar{b})\,H(\gamma\gamma)$, $\lambda_{3H}=1$	941.37 ± 7.65	723.86 ± 6.64	217.51 ± 3.66	0.30 ± 0.006	3×10^5
$H(b\bar{b})\,H(\gamma\gamma)$, $\lambda_{3H}=2$	557.36 ± 1.93	431.45 ± 1.87	125.91 ± 1.21	0.29 ± 0.003	3×10^5
$H(b\bar{b})\,H(\gamma\gamma)$, $\lambda_{3H}=6$	753.18 ± 6.02	566.18 ± 5.59	187.00 ± 5.33	0.33 ± 0.010	3×10^5
$H(b\bar{b})\,H(\gamma\gamma)$, $\lambda_{3H}=10$	3838.33 ± 36.82	2924.25 ± 32.11	914.08 ± 28.01	0.31 ± 0.010	3×10^5
$gg\,H(\gamma\gamma)$	890.47 ± 72.91	742.97 ± 58.43	147.50 ± 20.51	0.20 ± 0.03	10^6
$t\bar{t}\,H(\gamma\gamma)$	868.73 ± 8.53	659.33 ± 12.94	209.40 ± 7.04	0.32 ± 0.01	9.63×10^5
$Z\,H(\gamma\gamma)$	168.86 ± 5.91	122.91 ± 4.68	45.95 ± 1.69	0.37 ± 0.02	10^6
$b\bar{b}\,H(\gamma\gamma)$	9.82 ± 0.59	7.00 ± 0.58	2.82 ± 0.25	0.40 ± 0.05	10^6
$b\bar{b}\gamma\gamma$	770.42 ± 23.48	514.96 ± 20.81	255.46 ± 15.10	0.50 ± 0.04	1.1×10^7
$c\bar{c}\gamma\gamma$	222.88 ± 40.55	111.44 ± 32.55	111.44 ± 26.92	1.00 ± 0.38	1.1×10^7
$jj\gamma\gamma$	32.28 ± 3.23	20.98 ± 3.99	11.30 ± 2.34	0.54 ± 0.15	10^7
$b\bar{b}j\gamma$	1829.13 ± 75.08	1288.34 ± 45.27	540.79 ± 49.79	0.42 ± 0.04	1.1×10^7
$c\bar{c}j\gamma$	293.81 ± 40.11	216.49 ± 36.71	77.32 ± 32.97	0.36 ± 0.16	1.1×10^7
$b\bar{b}jj$	3569.73 ± 209.93	2294.83 ± 207.69	1274.90 ± 189.68	0.56 ± 0.10	3.43×10^6
$Z(b\bar{b})\gamma\gamma$	54.87 ± 3.79	35.72 ± 3.36	19.15 ± 2.02	0.54 ± 0.08	10^6
$t\bar{t}$ (≥ 1 leptons)	59.32 ± 7.40	38.32 ± 5.79	21.00 ± 5.61	0.55 ± 0.17	1.1×10^7
$t\bar{t}\gamma$ (≥ 1 leptons)	105.68 ± 8.22	62.53 ± 5.07	43.15 ± 7.95	0.69 ± 0.14	10^6
Total Background	8876.00 ± 243.07	6115.82 ± 227.41	2760.18 ± 202.67	0.45 ± 0.04	
Significance Z	9.823	9.082	4.087		
Combined significance		9.959			

the regions of 1-σ error, as shown in the right frame of Fig. 9.

The black-shaded region (delimited by the black dashed lines) in the right frame of Fig. 9 shows the 1-σ errors versus the input values of $\lambda_{3H}^{\rm in}$ with the luminosity of 3 ab^{-1}. Incidentally, the black solid line shows the center values of output λ_{3H} values or $\lambda_{3H}^{\rm out}$ along the $\lambda_{3H}^{\rm out}=\lambda_{3H}^{\rm in}$ line denoted by the thin dotted line. We note that there exists a bulk region of $2.6 \lesssim \lambda_{3H} \lesssim 4.8$ in which one cannot pin down the λ_{3H} coupling. We find that the bulk region reduces to $3.1 \lesssim \lambda_{3H} \lesssim 4.3$ assuming the luminosity of 30 ab^{-1} as shown by the red-shaded region (delimited by the red dashed lines) in the same frame of Fig. 9.

Even though it would be difficult to pin down the λ_{3H} coupling in the bulk region, yet one goes a bit away from it and is able to measure the coupling with a high precision as indicated by the narrowness of the 1-σ error regions. And, the two-fold ambiguity can be lifted up by exploiting the kinematical differences found in the distributions of $\Delta R_{\gamma\gamma}$, $P_T^{\gamma\gamma}$, $M_{\gamma\gamma bb}$ when λ_{3H} takes on different values: see Fig. 15. Keeping these all in mind, in Fig. 10, we show the regions in which one can determine the λ_{3H} coupling within an absolute error of 0.3 (either upper or lower error) along the $\lambda_{3H}^{\rm out}=\lambda_{3H}^{\rm in}$ line assuming 3 ab^{-1} (upper panel) and 30 ab^{-1} (lower panel). The green-shaded regions around $\lambda_{3H}=3.5$ denote the bulk regions. We observe that, when $\lambda_{3H} \lesssim 1.6\,(2.4)$ or $\lambda_{3H} \gtrsim 5.9\,(5.3)$, one can pin down the λ_{3H} coupling with an absolute error smaller than 0.3 assuming 3 (30) ab^{-1}. At the SM value of $\lambda_{3H}=1$, specifically, we observe that the coupling can be measured with about 20 (7) % accuracy assuming the integrated luminosity of 3 (30) ab^{-1}. Our results are about 2 times better than those reported in Ref. [39] and comparable with those in Ref. [40] taking account of the more sophisticated and comprehensive treatment of the background processes taken in this work.

Before moving to the next Section, we would like to comment that the bulk region can be shifted by adopting a different set of selection cuts and it may help if it turns out that λ_{3H} falls into the bulk region in future.

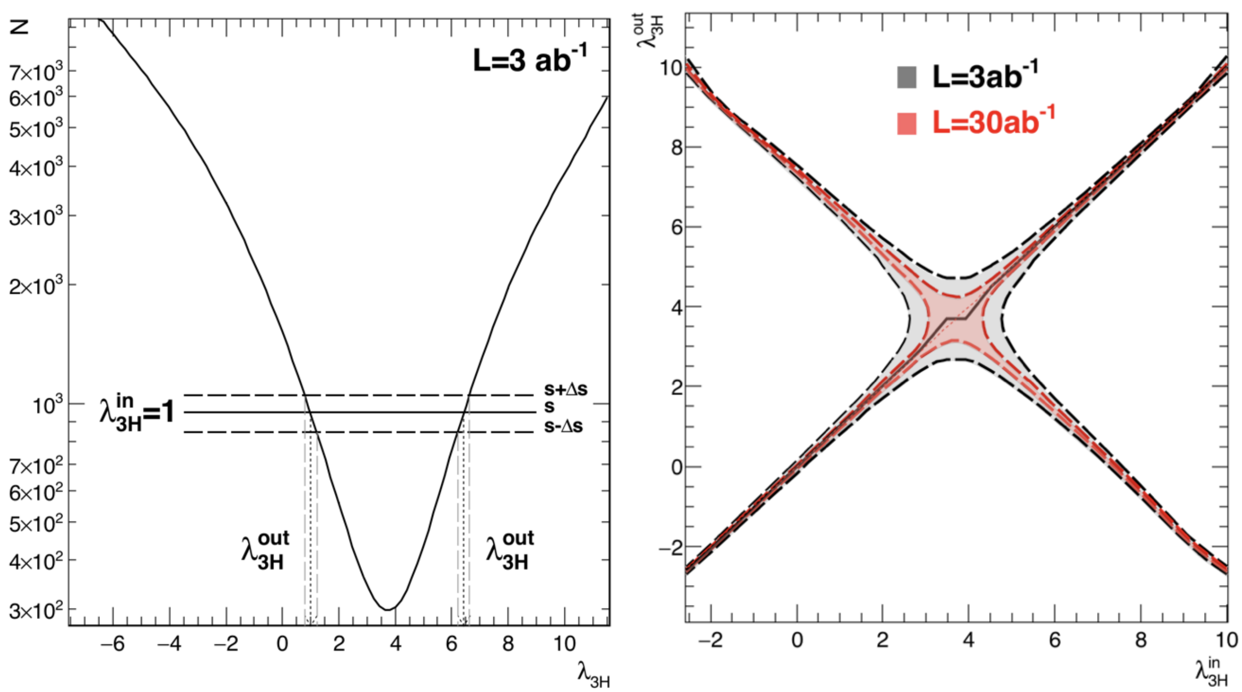

FIG. 9. **HL-100 TeV**: (Left) The number of signal events N versus λ_{3H} with 3 ab^{-1}. The horizontal solid line is for the number of signal events s when $\lambda_{3H}^{\rm in} = 1$ and the dashed lines for $s \pm \Delta s$ with the statistical error of $\Delta s = \sqrt{s+b}$. (Right) The 1-σ error regions versus the input values of $\lambda_{3H}^{\rm in}$ assuming 3 ab^{-1} (black) and 30 ab^{-1} (red).

V. FURTHER IMPROVEMENTS ENVISAGED

In our analysis, we are taking the SM cross sections of $\sigma(gg \to HH) = 45.05$ fb and $\sigma(gg \to HH) = 1749$ fb at 14 TeV and 100 TeV, respectively, which are calculated at NNLO accuracy including NNLL gluon resummation in the infinite top quark mass approximation. We have taken these values of cross sections to confirm, especially, the ATLAS results [30]. Recently, the NLO corrections considering full top-quark mass dependence have been available [41, 42]. The calculation reveals that the full top-quark mass dependence is vital to get reliable predictions for Higgs boson pair production. Precisely, the total cross section is reduced by 14 % at 14 TeV compared to that obtained by the Born improved Higgs Effective Field Theory (HEFT) in which the infinite top mass approximation is taken. At 100 TeV, the larger reduction of 24 % is found.

At the moment, as suggested in Ref. [43], the best way to incorporate the finite top-quark mass effects at NNLO might be by adopting the FT approximation [16, 44] in which the full top-quark mass dependence is considered only in the real radiation while the HEFT is taken in the virtual part. At NNLO in the FT approximation, $\sigma(gg \to HH) = 36.69$ fb and $\sigma(gg \to HH) = 1224$ fb at 14 TeV and 100 TeV, respectively [43]. We observe that 20 (30) % reduction at 14 (100) TeV compared to the cross sections used in Sections III and IV. To see the impact of the reduced cross sections on our main results, in Fig. 11, we show the signal significance over the background versus λ_{3H} at the HL-LHC (left) and the regions in which one can determine the λ_{3H} coupling with an absolute error of 0.3 at the HL-100 TeV collider (right). At 14 TeV with 3000 fb^{-1}, the trilinear coupling is constrained to be $-1.5 < \lambda_{3H} < 8.1$ at 95% CL taking account of the uncertainties associated with the top-Yukawa coupling and the estimation of backgrounds. Taking the central line, the 95% CL sensitivity region for λ_{3H} is $-0.4 < \lambda_{3H} < 7.5$ which becomes broader by the amount of ± 0.4 compared to the results presented in Section III [12]. At 100 TeV, we find a little bit broader bulk regions of $2.4 \lesssim \lambda_{3H} \lesssim 5.0$ and $3.0 \lesssim \lambda_{3H} \lesssim 4.4$ with 3 ab^{-1} and 30 ab^{-1}, respectively, compared to the results presented in Section IV [13]. And, λ_{3H} can be measured with an accuracy of 30 (10) % with an integrated luminosity of 3 (30) ab^{-1} when it takes on its SM value of 1. We observe that the effects of the reduced cross sections are less

[12] Recall that the corresponding region is $0 < \lambda_{3H} < 7.1$ if the NNLO+NNLL cross section of 45.05 fb is taken.

[13] Recall that, when the NNLO+NNLL cross section of 1749 fb is taken at 100 TeV, the bulk regions are $2.6\,(3.1) < \lambda_{3H} < 4.8\,(4.3)$ and λ_{3H} can be measured with an accuracy of 20 (7) % at its SM value with 3 ab^{-1} (30 ab^{-1}).

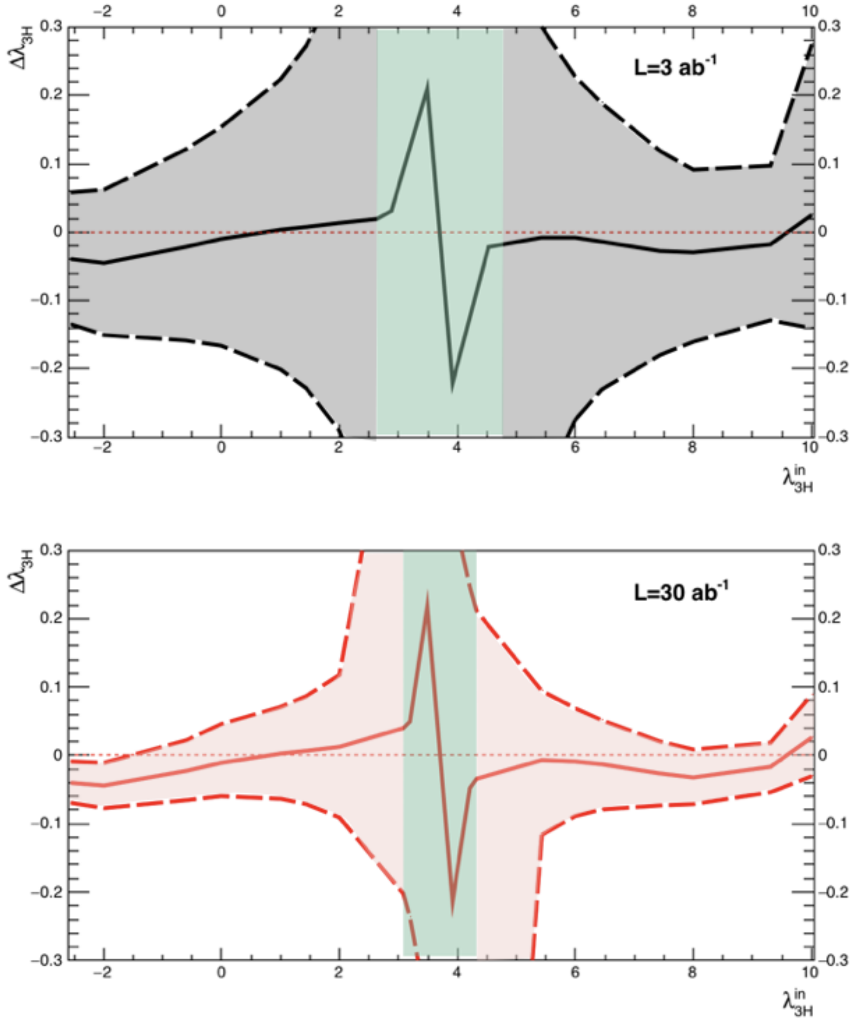

FIG. 10. **HL-100 TeV**: $\Delta\lambda_{3H} = \lambda_{3H}^{\rm out} - \lambda_{3H}^{\rm in}$ versus $\lambda_{3H}^{\rm in}$ along the $\lambda_{3H}^{\rm out} = \lambda_{3H}^{\rm in}$ line with 3 ab^{-1} (upper) and 30 ab^{-1} (lower). The lines are the same as in the right frame of Fig. 9. We consider $|\Delta\lambda_{3H}| \leq 0.3$ to find the regions in which one can pin down the λ_{3H} coupling with an absolute error smaller than 0.3.

significant in the case with 30 ab^{-1} at 100 TeV in which the number of signal events is comparable to or larger than that of backgrounds.

The QCD corrections also affect the ratio $\sigma(gg \to HH)/\sigma(gg \to HH)_{\rm SM}$ which is used to obtain the cross sections for non-SM values of λ_{3H}. The QCD corrections depend on λ_{3H} and become larger when λ_{3H} deviates from the SM value 1 due to the nontrivial interference between the triangle and box diagrams [42]. We observe that the ratio increases by about 10 (35) % at $\lambda_{3H} = -1\,(5)$, see Fig. 12. It is clear that the QCD corrections are less significant than the uncertainties associated with the top-Yukawa coupling, see Fig. 2. In this respect, we have not taken account of the λ_{3H}-dependent QCD corrections on the ratio $\sigma(gg \to HH)/\sigma(gg \to HH)_{\rm SM}$ in this work [14]. On the other hand, when $|\lambda_{3H}|$ is significantly larger than 1, vertex corrections proportional to λ_{3H}^3 appear at the amplitude level. This may bring sizeable distortion to $\sigma(gg \to HH)/\sigma(gg \to HH)_{\rm SM}$. In this case, it might be practical to consider λ_{3H} as an effective parameter, not as a fundamental one.

Note that the $P_T^{\gamma\gamma,bb}$ and $M_{\gamma\gamma bb}$ distributions are affected by the QCD corrections at NLO and NNLO as shown in, for example, Refs. [42, 43]. For more precise predictions at the HL-LHC and HL-100 TeV collider and to lift up the two-fold ambiguity in λ_{3H} especially, one may need to incorporate them in the future.

---

[14] Taking account of the λ_{3H}-dependent QCD corrections, at 14 TeV, we observe that the central 95% CL sensitivity region reduces from $-0.4 < \lambda_{3H} < 7.5$ to $-0.4 < \lambda_{3H} < 6.9$ since the QCD corrections enhance the signal cross section for $\lambda_{3H} \lesssim 1$ and $\lambda_{3H} \gtrsim 2.5$.

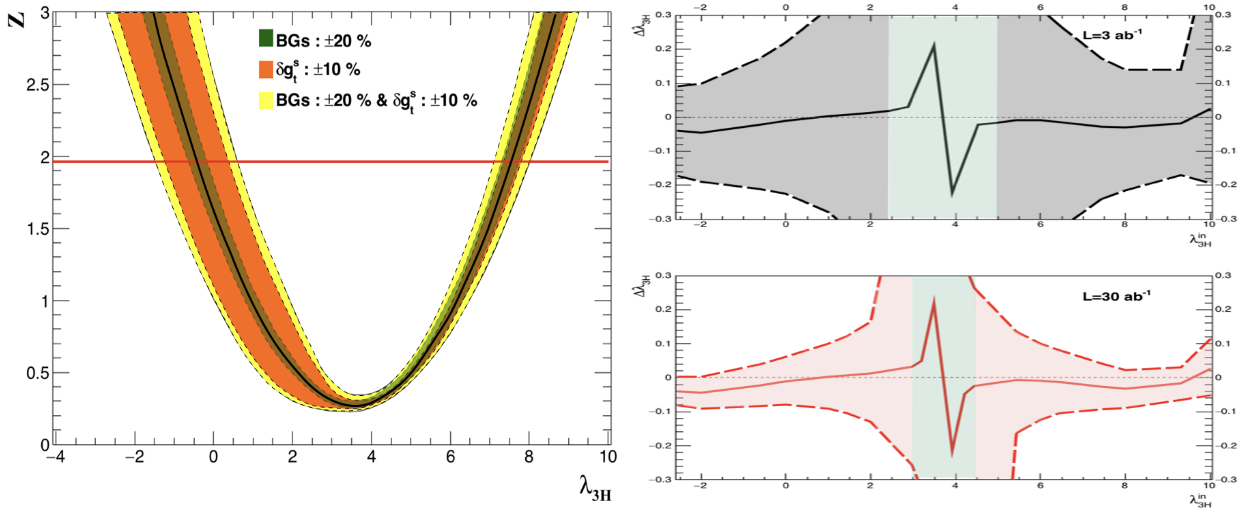

FIG. 11. (Left) **HL-LHC**: The same as in Fig. 6 but taking the NNLO cross section $\sigma(gg \to HH) = 36.69$ fb in the FT approximation. (Right) **HL-100 TeV**: The same as in Fig. 10 but taking the NNLO cross section $\sigma(gg \to HH) = 1224$ fb in the FT approximation.

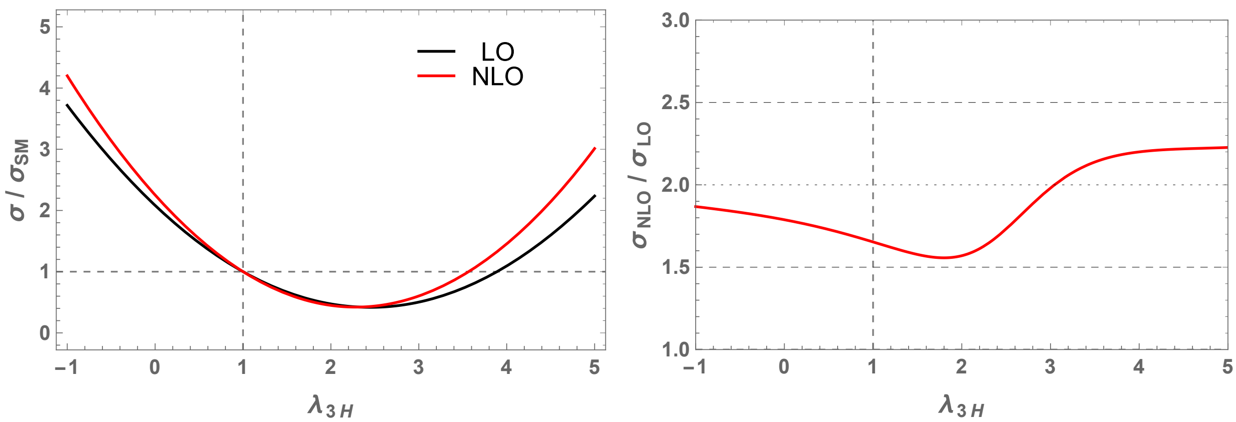

FIG. 12. (Left) The ratio $\sigma(gg \to HH)/\sigma(gg \to HH)_{\rm SM}$ versus λ_{3H} at LO (black) and NLO (red) at 14 TeV. We have taken the NLO cross sections considering full top-quark mass dependence. (Right) The ratio $\sigma^{\rm NLO}(gg \to HH)/\sigma^{\rm LO}(gg \to HH)$ versus λ_{3H} at 14 TeV. We refer to Ref. [42] for absolute cross sections as functions of λ_{3H}.

The PDF set of `CTEQ6L1` taken to calculate the non-resonant backgrounds does not include the use of data from LHC experiments. To study the impact of the LHC data on PDF, instead of `CTEQ6L1`, we take the PDF set of `CT14LO` [45] and re-simulate all the non-resonant backgrounds at 14 TeV. Taking the example of $b\bar{b}\gamma\gamma$ background, which is one of the two most severe non-resonant backgrounds, we obtain the overall efficiency of 4.34×10^{-3} by generating 10^7 events. This is very similar to the efficiency of 4.49×10^{-3} obtained using `CTEQ6L1`, see Table XIII. Actually, we observe that the two efficiencies in each step of cut flow coincide within less than 10% and there are no significant differences in kinematic distributions caused by `CT14LO`. Meanwhile, the real effect of `CT14LO` is the reduction of the cross sections for the non-resonant backgrounds. For $b\bar{b}\gamma\gamma$, as an example, it reduces to 112 fb [15]. Compared to the cross section of 140 fb obtained using `CTEQ6L1`, the cross section reduces by 20%.

Furthermore, the pre-selection cuts listed in Eq. (6) may not be enough to avoid the double counting problems in the non-resonant background samples. To address this point, we implement MLM matching [46, 47]. We observe that there are no significant differences in kinematic distributions due to MLM matching. For details of the matching precesses and the calculation of the merged cross sections, we refer to Appendix C. Taking account of the NNLO cross section $\sigma(gg \to HH) = 36.69$ fb in the FT approximation and the λ_{3H}-dependent QCD corrections, we obtain the central

---

[15] For other backgrounds at 14 TeV, see $\sigma_{\rm Eq.\,(6)}$ presented in Table. XV.

95% CL sensitivity region of $-0.4 < \lambda_{3H} < 6.9$ at 14 TeV, see the black dash-dotted line in Fig. 21. Incorporating the impact of `CT14LO` and the reduction of the non-resonant background cross sections by MLM matching, the region reduces to $0.1 < \lambda_{3H} < 6.6$, see the blue dashed line in Fig. 21.

Last but not least, we also take into account the contribution from the Higgs production accompanied by a hard $b\bar{b}$ pair via gluon-fusion at 14 TeV. For this purpose, we calculate the $gg \to Hb\bar{b}$ process, which is supposed to be the leading hard process for the contribution [13]. Adopting the cuts suggested in Ref [13] and using `MG5_aMC@NLO` and `NNPDF2.3LO`, we obtain $\sigma(gg \to Hb\bar{b}) \simeq 4.8$ fb at 14 TeV [16]. Then we find a selection efficiency of 2.7% for the process $gg \to H(\to \gamma\gamma)b\bar{b}$, which leads to 0.9 event at 14 TeV with 3 ab^{-1} after all the selection cuts are applied. Therefore, the total number of the $ggH(\to \gamma\gamma)$ background may increase into $6.6 + 0.9 = 7.5$ after including the hard process. We conclude that about 10% of the background might come from the hard $b\bar{b}$ pair production at 14 TeV.

VI. CONCLUSIONS

One of the major goals of the HL-LHC and HL-100 TeV hadron collider is to unfold the mystery of the EWSB mechanism, which is related to the origin of mass. We have investigated the trilinear self-coupling of the Higgs boson in Higgs-pair production using the most promising channel $pp \to HH \to \gamma\gamma b\bar{b}$ with a fully comprehensive signal-background analysis. It turns out that various fake backgrounds, including $c \to b$, $j \to \gamma$, $e \to \gamma$, are among the most dominant backgrounds that have to be discriminated against the signal.

The high-luminosity option of the LHC (HL-LHC) with an integrated luminosity of 3000 fb^{-1} can only constrain the trilinear coupling by $-1.0 < \lambda_{3H} < 7.6$ at 95% CL after taking into account the uncertainties associated with the top-Yukawa coupling and estimation of total background. This is unfortunate if the trilinear coupling takes on the SM value, it cannot be confirmed at the HL-LHC due to very small event rates. On the other hand, a much larger signal event rate at the HL-100 hadron collider enables one to pin down the value of λ_{3H} with an absolute error smaller than 0.3, except for a near-bulk region $1.6 < \lambda_{3H} < 5.9$ ($2.4 < \lambda_{3H} < 5.3$), with an integrated luminosity of 3 ab^{-1} (30 ab^{-1}). If λ_{3H} takes on the SM value, it can be measured with an accuracy of 20 (7) % with luminosity of 3 (30) ab^{-1}.

Before closing we would like to offer a few more comments.

1. Variations of cross sections with λ_{3H} for different production channels differ from one another. Indeed, if λ_{3H} falls at the minimum of $\sigma(gg \to HH)$, one can use, for example, $q\bar{q}^{(\prime)} \to W/Z + HH$ to probe the trilinear coupling. See Fig. 1.

2. We do not investigate the vector-boson fusion mechanism in this work. Though its cross section is at least one order magnitude smaller than gluon fusion, it has an additional handle to discriminate against backgrounds due to two very energetic and forward jets in the final state.

3. Currently, the reconstruction of the b-quark momentum is far from ideal as can be shown from the invariant mass $M_{b\bar{b}}$ spectrum. We expect that the b-jet tagging and b-jet reconstruction can be substantially improved with Deep Learning techniques in future, such that the invariant mass cut on $M_{b\bar{b}}$ can be much more effective.

4. In many other Higgs-sector extensions of the SM, there usually exist heavy neutral scalar bosons, which can be produced via gluon fusion and decays into Higgs-boson pair. Our approach of signal-background analysis can be adopted to analyze such kinds of models. Although specialized cuts tailored for particular models may generate higher significance, our approach can be applied in general.

5. Adopting the most recent NNLO calculations in the FT approximation, the inclusive cross section is reduced by 20 % at 14 TeV compared to the NNLO+NNLL cross section and, accordingly, the 95 % sensitivity range of λ_{3H} broadens by about 10 %. On the other hand, the inclusive cross section is reduced by 30 % at 100 TeV which results in about 20 % increment of bulk regions. And the accuracy at $\lambda_{3H} = 1$ worsens to 30 (10) % with 3 (30) ab^{-1}.

6. When we compare our HL-100 TeV results to those of Ref. [20], we found that their results have higher significance. This is because we have considered more backgrounds in our analysis such as the category of single-Higgs backgrounds and $bbjj$.

7. We observe that the non-resonant backgrounds could be significantly reduced by reflecting the impact of the LHC data on PDF and considering MLM matching.

[16] This is about 4 times smaller than the corresponding cross section of ~ 22 fb at 27 TeV [13].

ACKNOWLEDGMENT

We thank Tie-Jiun Hou for helpful comments on PDFs. We also thank Olivier Mattelaer and Stefan Prestel for helpful comments on MLM matching and DJR distribution in **MadGraph5_aMC@NLO** with PYTHIA8. This work was supported by the National Research Foundation of Korea (NRF) grant No. NRF- 2016R1E1A1A01943297. K.C. was supported by the MoST of Taiwan under grant number MOST-105-2112-M-007-028-MY3. J.P. was supported by the NRF grant No. NRF-2018R1D1A1B07051126.

Appendix A: Kinematical distributions for the signal and backgrounds at the HL-LHC and HL-100 TeV hadron collider

In Fig. 13, we show the $\Delta R_{\gamma\gamma}$, $P_T^{\gamma\gamma}$, $\Delta R_{\gamma b}$, and $M_{\gamma\gamma bb}$ distributions for the signal taking $\lambda_{3H} = -4, 0, 1, 2, 6$, and 10 at the HL-LHC. We observe the $M_{\gamma\gamma bb}$ distribution becomes narrower and softer for the larger values of $|\lambda_{3H}|$ due to the s-channel Higgs propagator.

In the left frame of Fig. 14, we show the angular separation between one of the photons and one of the b quarks at the HL-LHC for the SM signal ($\lambda_{3H} = 1$) and all the backgrounds considered in this work. The signal tends to have relatively larger $\Delta R_{\gamma b}$ implying that γ and b originated from the signal are more or less back-to-back. The right frame of Fig. 14 is for the invariant mass distributions $M_{\gamma\gamma bb}$.

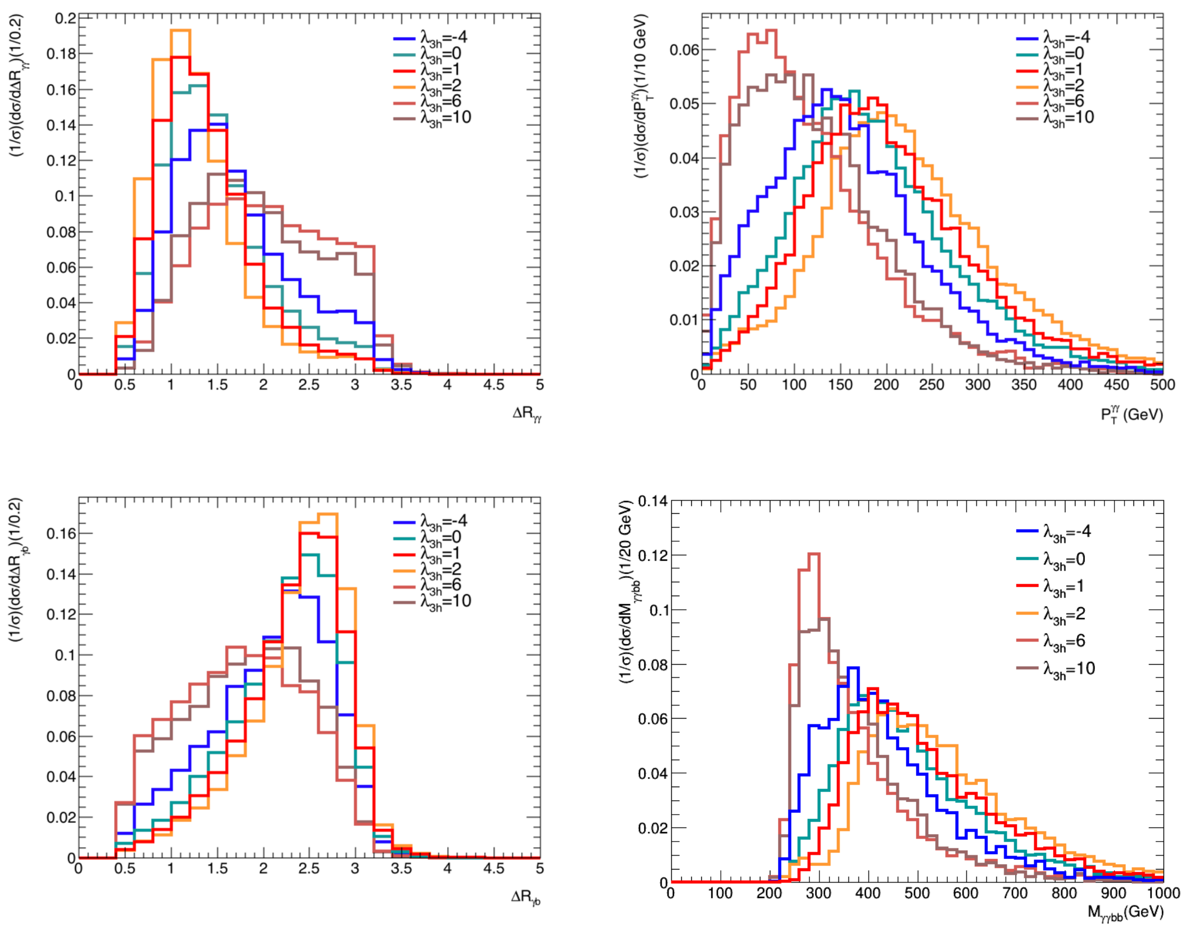

FIG. 13. **HL-LHC**: The $\Delta R_{\gamma\gamma}$, $P_T^{\gamma\gamma}$, $\Delta R_{\gamma b}$, and $M_{\gamma\gamma bb}$ distributions for the signal taking $\lambda_{3H} = -4, 0, 1, 2, 6$, and 10.

Fig. 15 is for some distributions at the HL-100 TeV hadron collider. The most of distributions are very similar to those at the HL-LHC.

Appendix B: Cut flow tables for all the backgrounds at the HL-LHC and HL-100 TeV hadron collider

In this appendix, we present the cut flow tables for all the backgrounds at the HL-LHC and HL-100 TeV hadron collider, see Tables XIII and XIV. We note that the lepton-veto cut does not affect the $t\bar{t}$ related BGs in which electrons are faking photons.

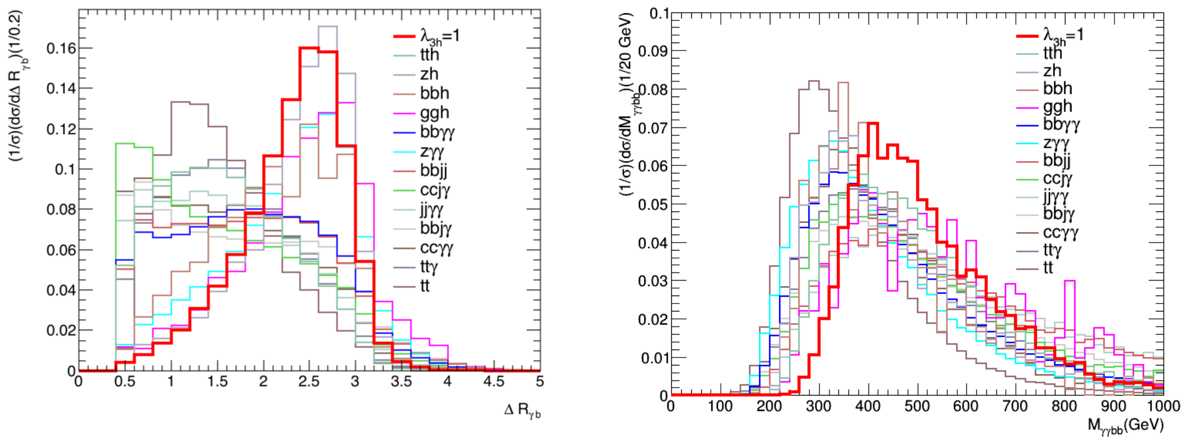

FIG. 14. **HL-LHC**: The $\Delta R_{\gamma b}$ and $M_{\gamma\gamma bb}$ distributions for the SM signal ($\lambda_{3H} = 1$) and all the backgrounds considered in this work.

Appendix C: On the cross sections of non-resonant backgrounds

For the non-resonant continuum backgrounds of $b\bar{b}\gamma\gamma$, $c\bar{c}\gamma\gamma$, $jj\gamma\gamma$, $b\bar{b}j\gamma$, $c\bar{c}j\gamma$, $b\bar{b}jj$ and $Z(b\bar{b})\gamma\gamma$, we have estimated the cross sections by applying the generator-level pre-selection cuts listed in Eq. (6). As explained in the main text, in each background, we consider a process with an additional hard parton[17] at the matrix-element level to capture the bulk of the NLO corrections.

In our estimation, there might be a worry of double counting between the leading process and the sub-leading one with an additional hard parton when generated background event samples are interfaced with `PYTHIA8` for showering and hadronization. To study the double counting issue, taking the PDF set of `CT14LO`, we consider the following three types of cross sections:

- $\sigma_{\mathrm{Eq.(6)}}$ without matching: the cross section obtained by applying the generator-level pre-selection cuts listed in Eq. (6)
- $\sigma_{\mathbf{xqcut}}$ without matching: the cross section obtained by varying **xqcut**. The variation of **xqcut** affects the pre-selection cuts on P_{T_j}, M_{jj}, and ΔR_{jj}. Otherwise, the other pre-selection cuts remain the same as in Eq. (6).
- σ_{merged} with MLM matching: the cross section obtained after implementing MLM matching. The merged cross section depends on the parameters of **xqcut** and Q_{cut}. In the default `MG5_aMC@NLO` setting, when a value of **xqcut** is given, three merged cross sections are provided for the three values of $Q_{\mathrm{cut}}/$**xqcut**: 1.5, 2.25, and 3. For the representative value, the merged cross section with $Q_{\mathrm{cut}}/$**xqcut** $= 1.5$ is taken.

For further discussion, it is helpful to introduce the distance between the two objects (d_{ij}) and that between an object and the beam direction (d_{iB}). Here an object could stand for a hard parton at the matrix-element level, a showering soft parton, or a clustered jet. Precisely,

$$d_{ij} = \min\left(P_{T_i}^{2p}, P_{T_j}^{2p}\right)\frac{\Delta R_{ij}^2}{R^2}\ , \quad d_{iB} = P_{T_i}^{2p}\,, \tag{C1}$$

where the parameter R defines the jet size and the parameter p the jet algorithm used. In MLM matching, the k_T algorithm with $p = 1$ is used. We note that $\sqrt{d_{iB}}$ in the k_T algorithm is nothing but P_{T_i} or the transverse momentum of an object.

Roughly speaking, the calculation of the merged cross section proceeds as the following steps:

(i) generation of hard partons with $\sqrt{d_{ij}}\,, \sqrt{d_{iB}} >$ **xqcut** at the matrix-element level

[17] In this appendix, we use the term of 'parton' instead of 'jet' to make distinction from a clustered jet obtained by collecting several hard and soft partons.

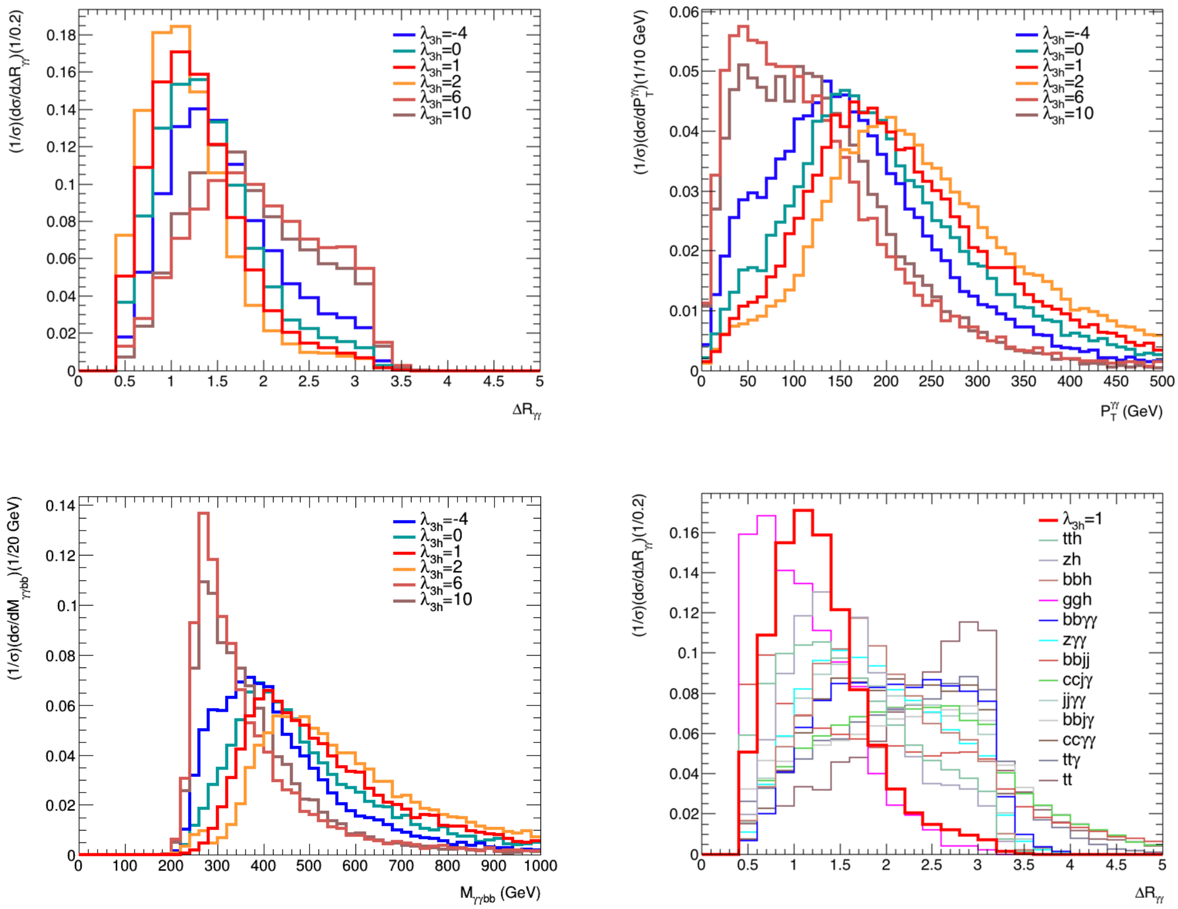

FIG. 15. **HL-100 TeV**: The $\Delta R_{\gamma\gamma}$ (upper left), $P_T^{\gamma\gamma}$ (upper right), and $M_{\gamma\gamma bb}$ (lower left) distributions for the signal taking $\lambda_{3H} = -4, 0, 1, 2, 6,$ and 10. In the lower right frame, the $\Delta R_{\gamma\gamma}$ distributions for the SM signal ($\lambda_{3H} = 1$) and all the backgrounds are compared.

(ii) showering soft partons with $\sqrt{d_{ij}}\,, \sqrt{d_{iB}} < \mu_F$ with μ_F being the factorization scale

(iii) clustering partons and pseudo-partons into jets according to a certain jet algorithm until all the distances among clustered jets and the beam direction are smaller than $Q^2_{\rm cut}$

(iv) matching by requiring that the number of jets obtained at the step (iii) should be equal to the number of hard partons at the step (i) [18] and the distance between a jet and its nearest hard parton is smaller than $\max\{Q^2_{\rm cut}, P_T^2\}$ with P_T being the transverse momentum of the nearest hard parton

(v) calculating the merged cross section by exploiting the weight factors and other information obtained in the matching step (iv)

In Table XV, we present the cross sections of $\sigma_{\rm Eq.(6)}$ and $\sigma_{\rm merged}$. For the three merged cross sections, $Q_{\rm cut}/{\rm GeV} =$ 30 (upper), 45 (middle), 60 (low) are taken with the parameter **xqcut** set to 20 GeV. Note that the smaller value of $Q_{\rm cut}$ usually results in the larger $\sigma_{\rm merged}$. First of all, we observe that $\sigma_{\rm Eq.(6)}$'s are smaller than those presented in Table I. This is because the PDF set of `CT14LO` is taken for this table while, in Table I, the PDF set of `CTEQ6L1` is taken. The difference between $\sigma_{\rm Eq.(6)}$ and $\sigma_{\rm merged}$ could be interpreted as the degree of double counting. Further, the variation of the merged cross sections depending on the choice of $Q_{\rm cut}$ may provide a measure of the quality of the

[18] Sometimes, for the highest multiplicity sample, the number of jets is required to be equal to or larger than the number of hard partons.

TABLE XIII. Cut flow table of the backgrounds in terms of efficiencies (%) at the HL-LHC.

	Single-Higgs BG				Non-resonant BG				
Cuts	ggH	$t\bar{t}H$	ZH	$b\bar{b}H$	$b\bar{b}\gamma\gamma$	$c\bar{c}\gamma\gamma$	$jj\gamma\gamma$	$b\bar{b}j\gamma$	$c\bar{c}j\gamma$
1. diphoton trigger	18.36	23.37	18.22	17.27	17.86	16.81	0.22	1.43×10^{-2}	0.02
2. ≥ 2 isolated photons	7.43	21.43	11.87	2.88	12.16	11.53	0.15	8.43×10^{-3}	0.01
3-1. jet candidates	1.97	20.33	5.49	0.25	7.33	6.82	0.09	7.75×10^{-3}	0.01
3-2 ≥ 2 two b-jet	1.99×10^{-2}	6.57	0.36	6.71×10^{-2}	2.13	0.24	2.60×10^{-3}	1.33×10^{-3}	1.98×10^{-4}
4. no. of jets ≤ 5	1.94×10^{-2}	5.16	0.36	6.70×10^{-2}	2.08	0.23	2.48×10^{-3}	1.23×10^{-3}	1.75×10^{-4}
5. lepton veto	1.91×10^{-2}	3.85	0.36	6.66×10^{-2}	2.07	0.23	2.42×10^{-3}	1.23×10^{-3}	1.71×10^{-4}
6. $\Delta R_{\gamma\gamma,bb}$ cut	1.13×10^{-2}	1.16	0.26	1.73×10^{-2}	0.41	0.03	7.71×10^{-4}	2.93×10^{-4}	3.29×10^{-5}
7-1. Higgs mass window $M_{\gamma\gamma}$	1.08×10^{-2}	1.09	0.25	1.71×10^{-2}	1.85×10^{-2}	1.08×10^{-3}	3.56×10^{-5}	8.30×10^{-6}	9.35×10^{-7}
7-2. Higgs mass window M_{bb}	1.92×10^{-3}	0.37	5.39×10^{-2}	4.20×10^{-3}	4.85×10^{-3}	2.20×10^{-4}	1.14×10^{-5}	2.33×10^{-6}	2.65×10^{-7}
8. $p_{T_{\gamma\gamma}}$, $p_{T_{bb}}$	1.83×10^{-3}	0.32	5.38×10^{-2}	3.90×10^{-3}	4.49×10^{-3}	2.10×10^{-4}	6.88×10^{-6}	1.71×10^{-6}	1.75×10^{-7}
other/barrel ratio	46.6%	34.5%	48.3%	39.6%	69.1%	57.2%	110.0%	80.4%	40.1%

TABLE XIII (continued)

	Non-resonant BG		$t\bar{t}$ related BG	
Cuts	$b\bar{b}jj$	$Z(b\bar{b})\gamma\gamma$	$t\bar{t}$	$t\bar{t}\gamma$
1. diphoton trigger	7.33×10^{-6}	18.70	21.25	6.00
2. ≥ 2 isolated photons	3.90×10^{-7}	13.01	9.97	4.77
3-1. jet candidates	3.90×10^{-7}	6.11	8.86	4.18
3-2 ≥ 2 two b-jet	4.01×10^{-7}	1.24	2.23	1.21
4. no. of jets ≤ 5	2.85×10^{-7}	1.22	2.07	1.09
5. lepton veto	2.80×10^{-7}	1.21	2.07	1.09
6. $\Delta R_{\gamma\gamma,bb}$ cut	8.76×10^{-8}	0.58	0.37	0.18
7-1. Higgs mass window $M_{\gamma\gamma}$	2.77×10^{-9}	2.64×10^{-2}	0.01	5.86×10^{-3}
7-2. Higgs mass window M_{bb}	6.98×10^{-10}	5.89×10^{-3}	3.79×10^{-3}	1.98×10^{-3}
8. $p_{T_{\gamma\gamma}}$, $p_{T_{bb}}$	4.25×10^{-10}	5.80×10^{-3}	2.40×10^{-3}	1.74×10^{-3}
other/barrel ratio	45.4%	66.6%	63.8%	57.6%

matching. For quantitative estimation of the matching quality, we introduce the following quantity:

$$\frac{\delta\sigma}{\sigma} \equiv \frac{\left|\sigma_{\rm merged}^{Q_{\rm cut}/{\rm xqcut}=1.5} - \sigma_{\rm merged}^{Q_{\rm cut}/{\rm xqcut}=3}\right|}{\sigma_{\rm merged}^{Q_{\rm cut}/{\rm xqcut}=1.5}}\,.$$

We observe $\delta\sigma/\sigma$ is less than about 2% for $b\bar{b}\gamma\gamma$, $c\bar{c}\gamma\gamma$, and $Z(b\bar{b})\gamma\gamma$ and it is about 40% for $b\bar{b}j\gamma$, $c\bar{c}j\gamma$, and $jj\gamma\gamma$. For $b\bar{b}jj$, on the other hand, it amounts to more than 80%.

Fig. 16 shows the ratios of $\sigma_{\mathbf{xqcut}}/\sigma_{\rm Eq.(6)}$ and $\sigma_{\rm merged}/\sigma_{\rm Eq.(6)}$ as functions of **xqcut** for the non-resonant backgrounds of $b\bar{b}\gamma\gamma$ (upper left), $c\bar{c}\gamma\gamma$ (upper right), and $Z(b\bar{b})\gamma\gamma$ (lower). In each frame, the dotted curve is for $\sigma_{\mathbf{xqcut}}/\sigma_{\rm Eq.(6)}$ and the band with a dashed line at its center for $\sigma_{\rm merged}/\sigma_{\rm Eq.(6)}$. A band is delimited by the choices of $Q_{\rm cut}/\mathbf{xqcut} = 1.5$ and 3 while the center line is obtained by taking $Q_{\rm cut}/\mathbf{xqcut} = 2.25$. For a given value of **xqcut**, the larger value of $Q_{\rm cut}$ usually leads to the smaller merged cross section. First of all, we observe that $\sigma_{\mathbf{xqcut}} = \sigma_{\rm Eq.(6)}$ around **xqcut** $\simeq 20$ GeV which is nothing but the value of P_{T_j} cut, see Eq. 6. And $\sigma_{\rm merged}$ is always smaller than $\sigma_{\mathbf{xqcut}}$ and the difference between them could be interpreted as the degree of double counting. We note that the difference becomes smaller when **xqcut** grows. This is because the leading process without an additional hard parton dominates more and more as the value of **xqcut** becomes large. For the choice of $Q_{\rm cut}/\mathbf{xqcut} = 1.5$ and $\mathbf{xqcut} = 20$ GeV, compared to $\sigma_{\mathbf{xqcut}}$, the merged cross sections for $b\bar{b}\gamma\gamma$, $c\bar{c}\gamma\gamma$, and $Z(b\bar{b})\gamma\gamma$ decrease by about 30%. Incidentally, we note the band widths are negligible for $b\bar{b}\gamma\gamma$, $c\bar{c}\gamma\gamma$, and $Z(b\bar{b})\gamma\gamma$.

Fig. 17 shows the ratios of $\sigma_{\mathbf{xqcut}}/\sigma_{\rm Eq.(6)}$ and $\sigma_{\rm merged}/\sigma_{\rm Eq.(6)}$ as functions of **xqcut** for the non-resonant backgrounds of $b\bar{b}j\gamma$ (upper left), $c\bar{c}j\gamma$ (upper right), $jj\gamma\gamma$ (lower left) and $b\bar{b}jj$ (lower right). Compared to $b\bar{b}\gamma\gamma$, $c\bar{c}\gamma\gamma$, and $Z(b\bar{b})\gamma\gamma$ in Fig. 16, the reduction of the merged cross sections is larger and the band width is sizeable.

Figs. 18, 19, and 20 show the Differential Jet Rate (DJR) distributions after hadronization, multi-parton interactions (MPI), and decays for all the non-resonant backgrounds taking **xqcut**$= 20$ GeV and $Q_{\rm cut} = 30$ GeV. We observe

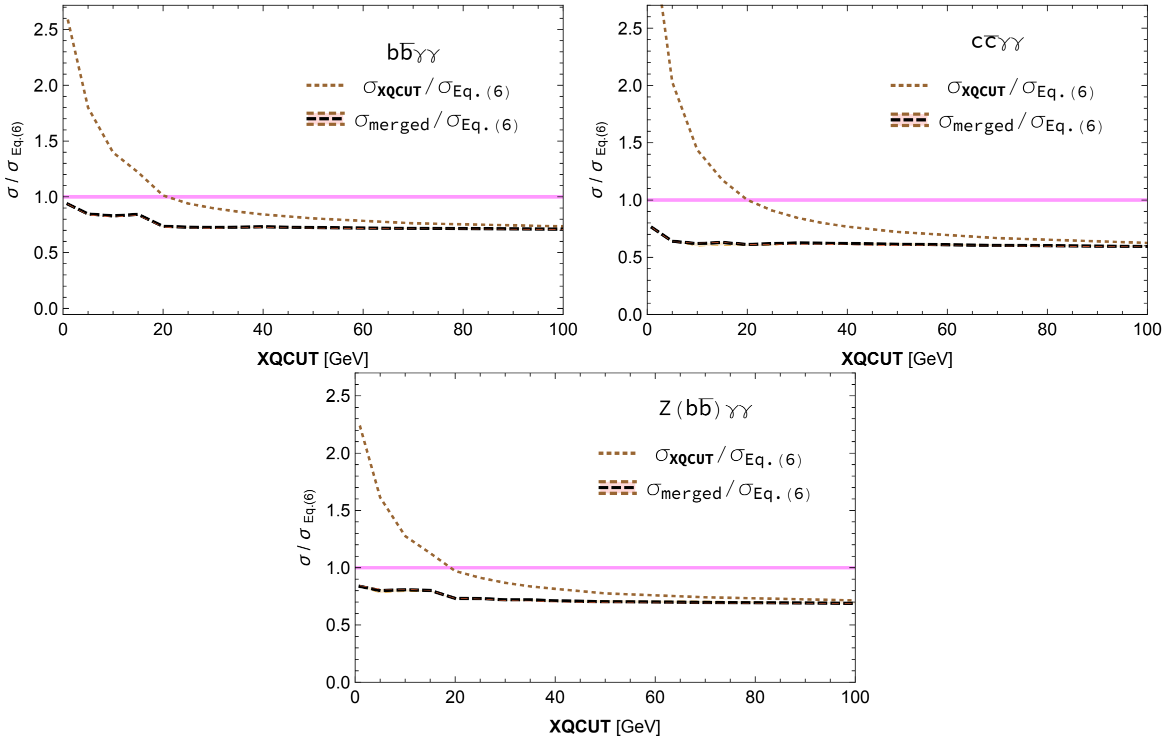

FIG. 16. The dependence of the ratios of $\sigma_{\mathbf{xqcut}}/\sigma_{\mathrm{Eq.(6)}}$ (dotted lines) and $\sigma_{\mathrm{merged}}/\sigma_{\mathrm{Eq.(6)}}$ (bands) on **xqcut** for the non-resonant backgrounds of $b\bar{b}\gamma\gamma$ (upper left), $c\bar{c}\gamma\gamma$ (upper right), and $Z(b\bar{b})\gamma\gamma$ (lower) . The horizontal magenta lines locate the positions where $\sigma_{\mathbf{xqcut}} = \sigma_{\mathrm{Eq.(6)}}$. The bands show the variation of the merged cross sections depending on the choice of $Q_{\mathrm{cut}}/\mathbf{xqcut}$: 1.5, 3 (upper and lower boundaries) and 2.25 (middle dashed line). The band width for all these 3 processes is negligible.

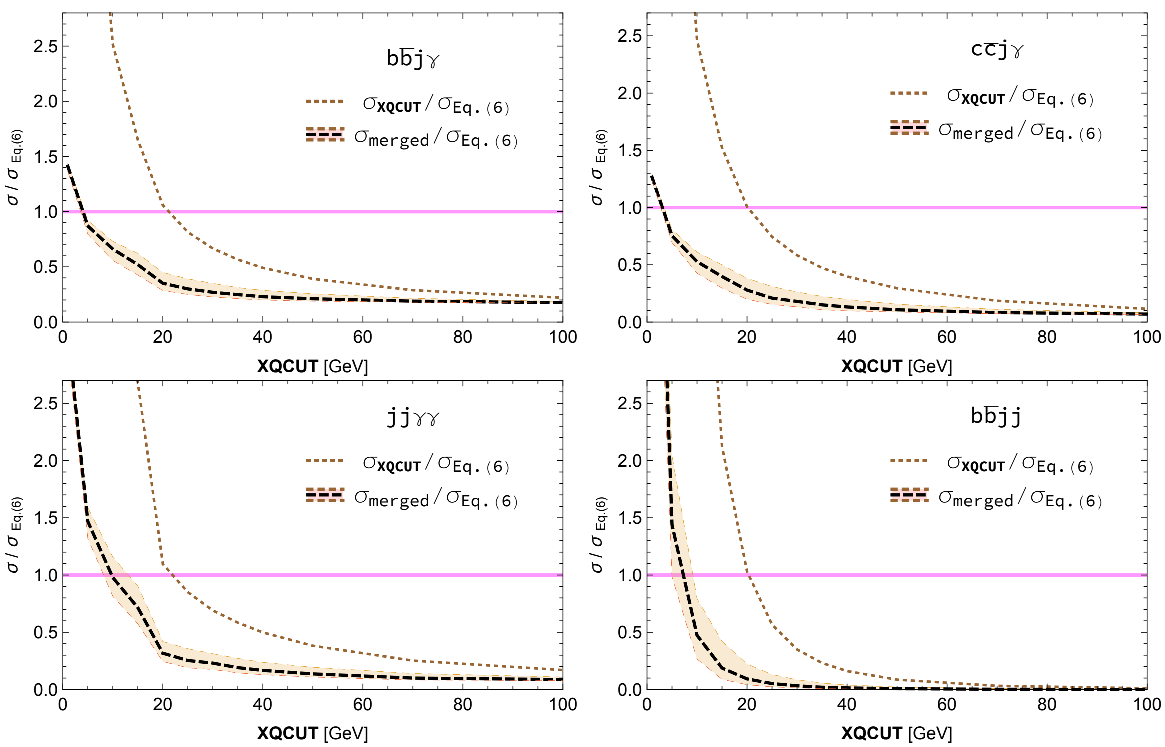

FIG. 17. The same as in Fig. 16 but for the the non-resonant backgrounds of $b\bar{b}j\gamma$ (upper left), $c\bar{c}j\gamma$ (upper right), $jj\gamma\gamma$ (lower left) and $b\bar{b}jj$ (lower right).

TABLE XIV. Cut flow table of the backgrounds in terms of efficiencies (%) at the HL-100 TeV hadron collider.

	Single-Higgs BG				Non-resonant BG				
Cuts	ggH	$t\bar{t}H$	ZH	$b\bar{b}H$	$b\bar{b}\gamma\gamma$	$c\bar{c}\gamma\gamma$	$jj\gamma\gamma$	$b\bar{b}j\gamma$	$c\bar{c}j\gamma$
1. diphoton trigger	60.04	45.79	54.04	64.18	44.55	44.13	0.33	0.08	7.58×10^{-2}
2. ≥ 2 isolated photons	22.87	31.53	22.91	11.97	15.44	16.85	0.09	0.03	2.73×10^{-2}
3-1. jet candidates	8.85	30.71	11.31	1.22	10.52	12.02	0.06	0.03	2.56×10^{-2}
3-2 ≥ 2 two b-jet	0.14	11.59	0.81	0.36	3.14	0.19	1.52×10^{-3}	0.01	4.19×10^{-4}
4. no. of jets ≤ 5	0.11	7.10	0.78	0.35	2.78	0.14	1.13×10^{-3}	4.35×10^{-3}	2.18×10^{-4}
5. lepton veto	0.11	5.20	0.78	0.35	2.78	0.14	1.13×10^{-3}	4.35×10^{-3}	2.18×10^{-4}
6. $\Delta R_{\gamma\gamma,bb}$ cut	0.10	3.79	0.71	0.19	1.62	0.08	7.78×10^{-4}	2.30×10^{-3}	1.03×10^{-4}
7-1. Higgs mass window $M_{\gamma\gamma}$	0.09	3.45	0.67	0.18	0.07	3.35×10^{-3}	3.23×10^{-5}	6.38×10^{-5}	3.29×10^{-6}
7-2. Higgs mass window M_{bb}	0.02	0.97	0.33	0.04	0.02	9.45×10^{-4}	8.20×10^{-6}	2.07×10^{-5}	1.08×10^{-6}
8. $p_{T_{\gamma\gamma}}$, $p_{T_{bb}}$	0.02	0.40	0.22	0.02	5.21×10^{-3}	1.64×10^{-4}	2.00×10^{-6}	4.23×10^{-6}	2.33×10^{-7}
other/barrel ratio	19.9%	31.8%	37.4%	40.3%	49.6%	100.0%	53.8%	42.0%	35.7%

TABLE XIV (continued)

	Non-resonant BG		$t\bar{t}$ related BG	
Cuts	$b\bar{b}jj$	$Z(b\bar{b})\gamma\gamma$	$t\bar{t}$	$t\bar{t}\gamma$
1. diphoton trigger	1.33×10^{-4}	45.38	14.61	10.49
2. ≥ 2 isolated photons	5.77×10^{-5}	14.85	5.98	5.62
3-1. jet candidates	5.77×10^{-5}	9.28	5.85	5.39
3-2 ≥ 2 two b-jet	1.01×10^{-5}	2.06	1.81	1.88
4. no. of jets ≤ 5	5.41×10^{-6}	1.92	1.28	1.32
5. lepton veto	5.41×10^{-6}	1.92	1.28	1.32
6. $\Delta R_{\gamma\gamma,bb}$ cut	3.17×10^{-6}	1.68	0.75	0.75
7-1. Higgs mass window $M_{\gamma\gamma}$	8.44×10^{-8}	0.07	0.02	0.02
7-2. Higgs mass window M_{bb}	2.79×10^{-8}	0.04	0.01	0.01
8. $p_{T_{\gamma\gamma}}$, $p_{T_{bb}}$	7.44×10^{-9}	0.02	1.31×10^{-3}	1.95×10^{-3}
other/barrel ratio	55.6%	53.6%	54.8%	69.0%

TABLE XV. **HL-LHC**: The cross sections for the non-resonant backgrounds taking the PDF set of `CT14LO`. For the three merged cross sections, $Q_{\rm cut}/{\rm GeV} = 30$ (upper), 45 (middle), 60 (low) are taken with the parameter **xqcut** set to 20 GeV.

Cross Section	$b\bar{b}\gamma\gamma$	$c\bar{c}\gamma\gamma$	$jj\gamma\gamma$	$b\bar{b}j\gamma$	$c\bar{c}j\gamma$	$b\bar{b}jj$	$Z(b\bar{b})\gamma\gamma$
$\sigma_{\rm Eq.(6)}$ [fb]	112	1081	1.40×10^4	2.72×10^5	0.91×10^6	3.00×10^8	5.03
$\sigma_{\rm merged}$ [fb]	82.5	647	0.59×10^4	1.22×10^5	0.35×10^6	0.67×10^8	3.65
	82.3	662	0.44×10^4	0.96×10^5	0.25×10^6	0.28×10^8	3.68
	81.5	662	0.34×10^4	0.78×10^5	0.18×10^6	0.13×10^8	3.68
$\delta\sigma/\sigma$ [%]	1.2	2.3	42	36	49	81	0.8

the DJR distributions for $b\bar{b}\gamma\gamma$, $c\bar{c}\gamma\gamma$, and $Z(b\bar{b})\gamma\gamma$ are very smooth and the variation of the merged cross sections depending on the choice of $Q_{\rm cut}$ is negligible. For $b\bar{b}j\gamma$, $c\bar{c}j\gamma$, and $jj\gamma\gamma$ the distributions are smooth and the variation is small. For $b\bar{b}jj$, the DJR distributions are coarse and the variation of the merged cross section is sizeable.

To conclude, the matching has been excellently implemented for $b\bar{b}\gamma\gamma$, $c\bar{c}\gamma\gamma$, and $Z(b\bar{b})\gamma\gamma$ backgrounds and it is less successful for $jj\gamma\gamma$, $b\bar{b}j\gamma$, and $c\bar{c}j\gamma$. On the other hand, for $b\bar{b}jj$, it is doubtful whether the merged cross section is trustworthy. Therefore, for $b\bar{b}\gamma\gamma$, $c\bar{c}\gamma\gamma$, and $Z(b\bar{b})\gamma\gamma$, one may safely use the merged cross sections obtained by matching the leading and sub-leading processes. For $jj\gamma\gamma$, $b\bar{b}j\gamma$, and $c\bar{c}j\gamma$, they are less reliable. And, for $b\bar{b}jj$, it might be recommended to use $\sigma_{\rm Eq.(6)}$ for conservative estimation of the background,

To see the impact of matching for the non-resonant backgrounds, we show the significance of the signal over the background versus λ_{3H} in Fig. 21. We find that the 95% CL region is reduced by the amount of about 15% taking the merged cross sections for the non-resonant backgrounds with `CT14LO`.

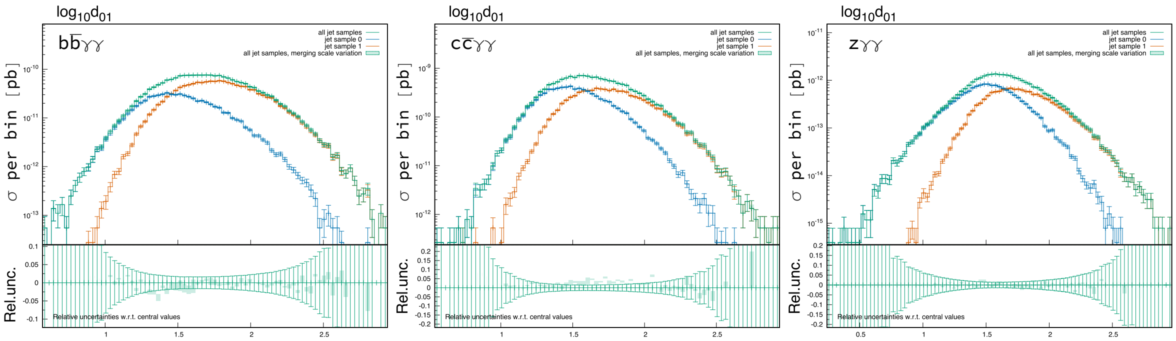

FIG. 18. **HL-LHC**: The Differential Jet Rate (DJR) distributions for the non-resonant backgrounds of $b\bar{b}\gamma\gamma$ (left), $c\bar{c}\gamma\gamma$ (middle), and $Z(b\bar{b})\gamma\gamma$ (right) taking **xqcut**= 20 GeV and $Q_{\rm cut}$ = 30 GeV. Here, "jet sample 0" and "jet sample 1" refer to the samples containing 0 and 1 hard parton, respectively, with $\sqrt{d_{ij}}\,, \sqrt{d_{iB}} >$ **xqcut** at the matrix-element level.

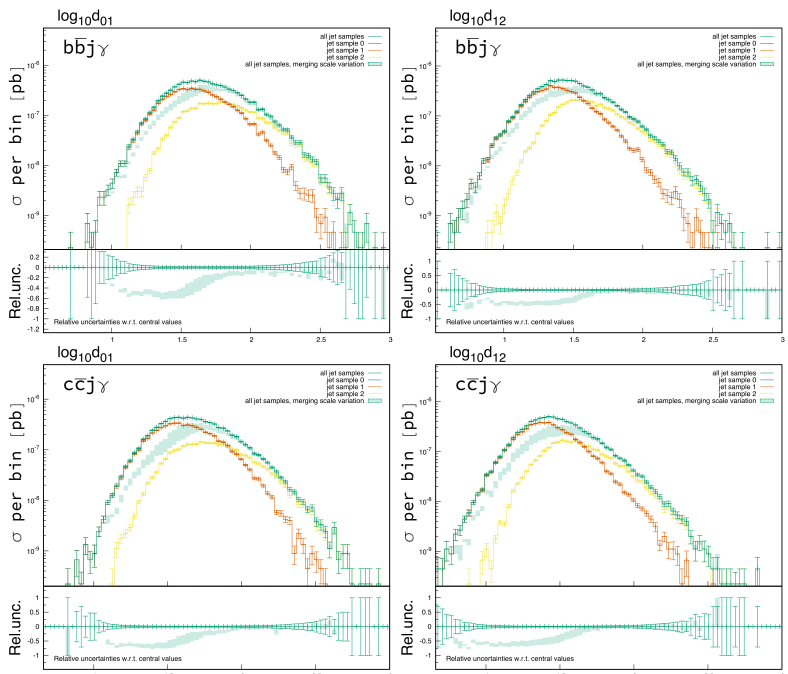

FIG. 19. **HL-LHC**: The DJR distributions for the non-resonant backgrounds of $b\bar{b}j\gamma$ (upper) and $c\bar{c}j\gamma$ (lower) taking **xqcut**= 20 GeV and $Q_{\rm cut}$ = 30 GeV. Here, "jet sample n" refers to the sample containing n hard partons at the matrix-element level.

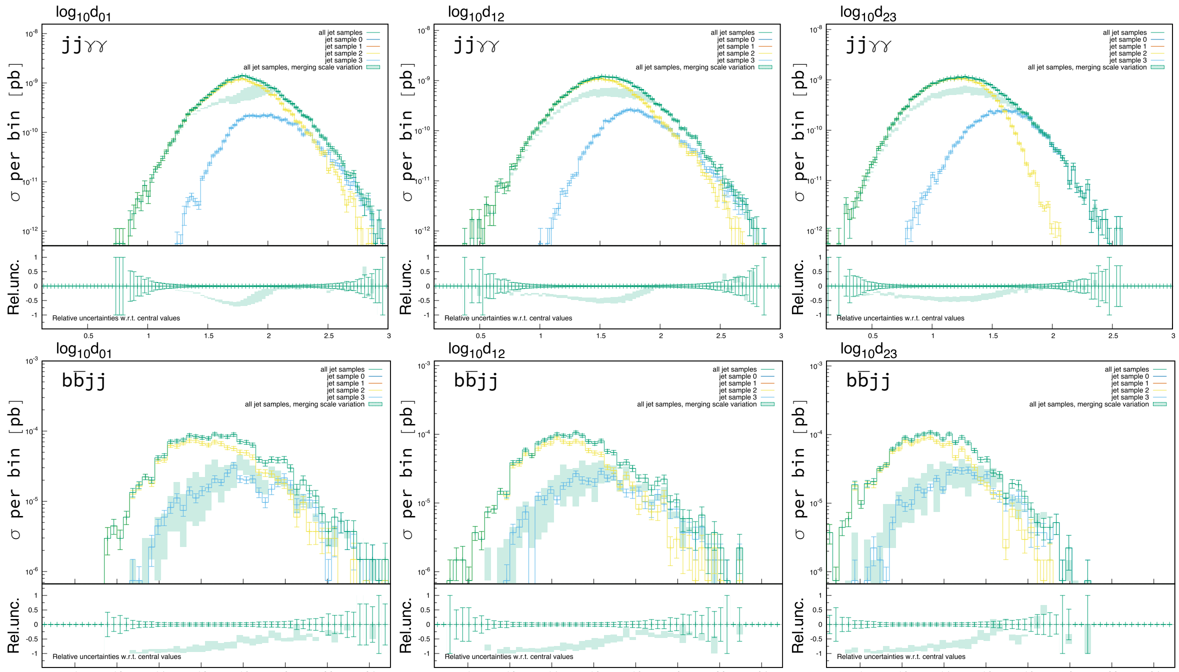

FIG. 20. **HL-LHC**: The DJR distributions for the non-resonant backgrounds of $jj\gamma\gamma$ (upper) and $b\bar{b}jj$ (lower) taking **xqcut**= 20 GeV and $Q_{\rm cut}$ = 30 GeV. Here, "jet sample n" refers to the sample containing n hard partons at the matrix-element level.

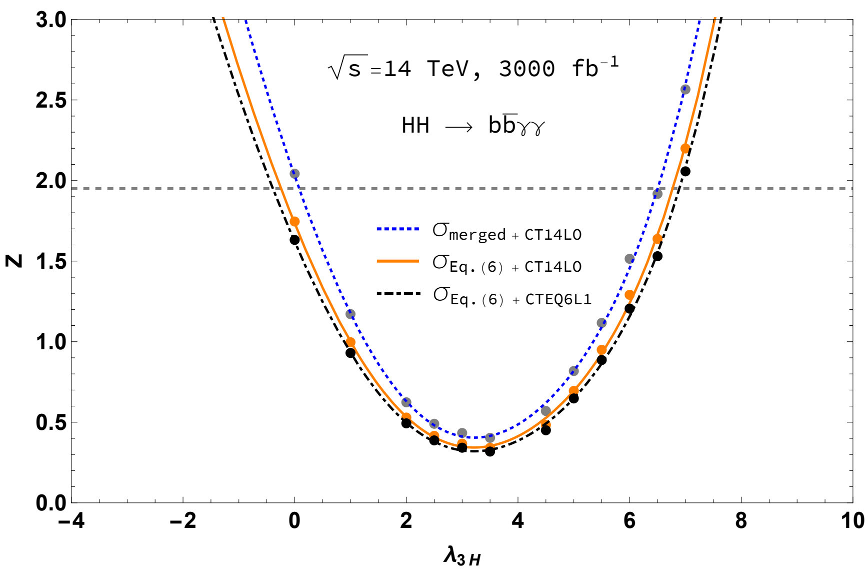

FIG. 21. **HL-LHC**: Significance of the signal over the background versus λ_{3H} taking $\sigma_{\rm Eq.(6)}$ (red solid) and $\sigma_{\rm merged}$ (blue dashed) for the non-resonant backgrounds. The PDF set of `CT14LO` is taken. For comparison, also shown is the case with the PDF set of `CTEQ6L1` (black dash-dotted). Note that the NNLO cross section $\sigma(gg \to HH) = 36.69$ fb in the FT approximation is taken and the λ_{3H}-dependent QCD corrections have been included, see Fig. 12.

[1] P. W. Higgs, "Broken Symmetries and the Masses of Gauge Bosons," Phys. Rev. Lett. **13**, 508 (1964); F. Englert and R. Brout, "Broken Symmetry and the Mass of Gauge Vector Mesons," Phys. Rev. Lett. **13**, 321 (1964); G. S. Guralnik, C. R. Hagen and T. W. B. Kibble, "Global Conservation Laws and Massless Particles," Phys. Rev. Lett. **13**, 585 (1964).

[2] G. Aad *et al.* [ATLAS Collaboration], "Observation of a new particle in the search for the Standard Model Higgs boson

with the ATLAS detector at the LHC," Phys. Lett. B **716**, 1 (2012) [arXiv:1207.7214 [hep-ex]]; S. Chatrchyan *et al.* [CMS Collaboration], "Observation of a new boson at a mass of 125 GeV with the CMS experiment at the LHC," Phys. Lett. B **716**, 30 (2012) [arXiv:1207.7235 [hep-ex]].

[3] K. Cheung, J. S. Lee and P. Y. Tseng, "Higgs Precision (Higgcision) Era begins," JHEP **1305** (2013) 134 doi:10.1007/JHEP05(2013)134 [arXiv:1302.3794 [hep-ph]]; K. Cheung, J. S. Lee and P. Y. Tseng, "Higgs precision analysis updates 2014," Phys. Rev. D **90** (2014) 095009 doi:10.1103/PhysRevD.90.095009 [arXiv:1407.8236 [hep-ph]].

[4] E. W. N. Glover and J. J. van der Bij, Nucl. Phys. B **309** (1988) 282. doi:10.1016/0550-3213(88)90083-1; D. A. Dicus, C. Kao and S. S. D. Willenbrock, Phys. Lett. B **203** (1988) 457. doi:10.1016/0370-2693(88)90202-X; T. Plehn, M. Spira and P. M. Zerwas, Nucl. Phys. B **479** (1996) 46 Erratum: [Nucl. Phys. B **531** (1998) 655] doi:10.1016/0550-3213(96)00418-X, 10.1016/S0550-3213(98)00406-4 [hep-ph/9603205]; A. Djouadi, W. Kilian, M. Muhlleitner and P. M. Zerwas, Eur. Phys. J. C **10** (1999) 45 doi:10.1007/s100529900083 [hep-ph/9904287]; S. Dawson, S. Dittmaier and M. Spira, Phys. Rev. D **58** (1998) 115012 doi:10.1103/PhysRevD.58.115012 [hep-ph/9805244]; U. Baur, T. Plehn and D. L. Rainwater, Phys. Rev. D **67** (2003) 033003 doi:10.1103/PhysRevD.67.033003 [hep-ph/0211224]; T. Binoth, S. Karg, N. Kauer and R. Ruckl, Phys. Rev. D **74** (2006) 113008 doi:10.1103/PhysRevD.74.113008 [hep-ph/0608057].

[5] U. Baur, T. Plehn and D. L. Rainwater, Phys. Rev. D **68** (2003) 033001 doi:10.1103/PhysRevD.68.033001 [hep-ph/0304015]: U. Baur, T. Plehn and D. L. Rainwater, Phys. Rev. Lett. **89** (2002) 151801 doi:10.1103/PhysRevLett.89.151801 [hep-ph/0206024]; U. Baur, T. Plehn and D. L. Rainwater, Phys. Rev. D **69** (2004) 053004 doi:10.1103/PhysRevD.69.053004 [hep-ph/0310056].

[6] J. Baglio, A. Djouadi, R. Grber, M. M. Mhlleitner, J. Quevillon and M. Spira, JHEP **1304**, 151 (2013) [arXiv:1212.5581 [hep-ph]]; J. Grigo, J. Hoff, K. Melnikov and M. Steinhauser, Nucl. Phys. B **875** (2013) 1 doi:10.1016/j.nuclphysb.2013.06.024 [arXiv:1305.7340 [hep-ph]]; V. Barger, L. L. Everett, C. B. Jackson and G. Shaughnessy, Phys. Lett. B **728** (2014) 433 doi:10.1016/j.physletb.2013.12.013 [arXiv:1311.2931 [hep-ph]]; W. Yao, arXiv:1308.6302 [hep-ph].

[7] C. Englert, F. Krauss, M. Spannowsky and J. Thompson, Phys. Lett. B **743**, 93 (2015) [arXiv:1409.8074 [hep-ph]]; T. Liu and H. Zhang, arXiv:1410.1855 [hep-ph]; D. E. Ferreira de Lima, A. Papaefstathiou and M. Spannowsky, JHEP **1408**, 030 (2014) [arXiv:1404.7139 [hep-ph]]; V. Barger, L. L. Everett, C. B. Jackson and G. Shaughnessy, Phys. Lett. B **728**, 433 (2014) [arXiv:1311.2931 [hep-ph]]; E. Asakawa, D. Harada, S. Kanemura, Y. Okada and K. Tsumura, Phys. Rev. D **82**, 115002 (2010) [arXiv:1009.4670 [hep-ph]]; A. Papaefstathiou, L. L. Yang and J. Zurita, Phys. Rev. D **87**, no. 1, 011301 (2013) [arXiv:1209.1489 [hep-ph]]; A. Papaefstathiou, arXiv:1504.04621 [hep-ph]; R. Frederix, S. Frixione, V. Hirschi, F. Maltoni, O. Mattelaer, P. Torrielli, E. Vryonidou and M. Zaro, Phys. Lett. B **732**, 142 (2014) [arXiv:1401.7340 [hep-ph]].

[8] K. Nishiwaki, S. Niyogi and A. Shivaji, JHEP **1404**, 011 (2014) [arXiv:1309.6907 [hep-ph]]; M. Gouzevitch, A. Oliveira, J. Rojo, R. Rosenfeld, G. P. Salam and V. Sanz, JHEP **1307**, 148 (2013) [arXiv:1303.6636 [hep-ph]]; M. J. Dolan, C. Englert and M. Spannowsky, JHEP **1210**, 112 (2012) [arXiv:1206.5001 [hep-ph]]; A. Azatov, R. Contino, G. Panico and M. Son, arXiv:1502.00539 [hep-ph]; N. Liu, S. Hu, B. Yang and J. Han, JHEP **1501**, 008 (2015) [arXiv:1408.4191 [hep-ph]]; F. Goertz, A. Papaefstathiou, L. L. Yang and J. Zurita, JHEP **1504**, 167 (2015) [arXiv:1410.3471 [hep-ph]]; R. Grober, M. Muhlleitner, M. Spira and J. Streicher, arXiv:1504.06577 [hep-ph]; F. Goertz, A. Papaefstathiou, L. L. Yang and J. Zurita, JHEP **1306**, 016 (2013) [arXiv:1301.3492 [hep-ph]]; R. Contino, M. Ghezzi, M. Moretti, G. Panico, F. Piccinini and A. Wulzer, JHEP **1208**, 154 (2012) [arXiv:1205.5444 [hep-ph]]; C. R. Chen and I. Low, Phys. Rev. D **90**, no. 1, 013018 (2014) [arXiv:1405.7040 [hep-ph]]; R. S. Gupta, H. Rzehak and J. D. Wells, Phys. Rev. D **88** (2013) 055024 doi:10.1103/PhysRevD.88.055024 [arXiv:1305.6397 [hep-ph]]; D. Goncalves, T. Han, F. Kling, T. Plehn and M. Takeuchi, arXiv:1802.04319 [hep-ph]; Q. H. Cao, B. Yan, D. M. Zhang and H. Zhang, Phys. Lett. B **752** (2016) 285 doi:10.1016/j.physletb.2015.11.045 [arXiv:1508.06512 [hep-ph]]; Q. H. Cao, G. Li, B. Yan, D. M. Zhang and H. Zhang, Phys. Rev. D **96** (2017) no.9, 095031 doi:10.1103/PhysRevD.96.095031 [arXiv:1611.09336 [hep-ph]]; H. J. He, J. Ren and W. Yao, Phys. Rev. D **93** (2016) no.1, 015003 doi:10.1103/PhysRevD.93.015003 [arXiv:1506.03302 [hep-ph]].

[9] S. Dawson, E. Furlan and I. Lewis, Phys. Rev. D **87**, no. 1, 014007 (2013) [arXiv:1210.6663 [hep-ph]]; M. Gillioz, R. Grober, C. Grojean, M. Muhlleitner and E. Salvioni, JHEP **1210** (2012) 004 [arXiv:1206.7120 [hep-ph]]; V. Barger, L. L. Everett, C. B. Jackson, A. Peterson and G. Shaughnessy, Phys. Rev. Lett. **114**, 011801 (2015) [arXiv:1408.0003 [hep-ph]]; M. J. Dolan, C. Englert and M. Spannowsky, Phys. Rev. D **87** (2013) 5, 055002 [arXiv:1210.8166 [hep-ph]]; G. D. Kribs and A. Martin, Phys. Rev. D **86**, 095023 (2012) [arXiv:1207.4496 [hep-ph]]; A. Arhrib, R. Benbrik, C. H. Chen, R. Guedes and R. Santos, JHEP **0908**, 035 (2009) [arXiv:0906.0387 [hep-ph]]; C. O. Dib, R. Rosenfeld and A. Zerwekh, JHEP **0605**, 074 (2006) [hep-ph/0509179]; R. Grober and M. Muhlleitner, JHEP **1106**, 020 (2011) [arXiv:1012.1562 [hep-ph]]; J. M. No and M. Ramsey-Musolf, Phys. Rev. D **89**, no. 9, 095031 (2014) [arXiv:1310.6035 [hep-ph]]; B. Hespel, D. Lopez-Val and E. Vryonidou, JHEP **1409**, 124 (2014) [arXiv:1407.0281 [hep-ph]]; S. M. Etesami and M. Mohammadi Najafabadi, Phys. Rev. D **92** (2015) no.7, 073013 doi:10.1103/PhysRevD.92.073013 [arXiv:1505.01028 [hep-ph]]; T. Corbett, A. Joglekar, H. L. Li and J. H. Yu, arXiv:1705.02551 [hep-ph].

[10] C. Han, X. Ji, L. Wu, P. Wu and J. M. Yang, JHEP **1404**, 003 (2014) [arXiv:1307.3790 [hep-ph]]; U. Ellwanger, JHEP **1308**, 077 (2013) [arXiv:1306.5541 [hep-ph]]; J. Cao, Z. Heng, L. Shang, P. Wan and J. M. Yang, JHEP **1304**, 134 (2013) [arXiv:1301.6437 [hep-ph]]; B. Bhattacherjee and A. Choudhury, Phys. Rev. D **91**, no. 7, 073015 (2015) [arXiv:1407.6866 [hep-ph]]; D. T. Nhung, M. Muhlleitner, J. Streicher and K. Walz, JHEP **1311** (2013) 181 doi:10.1007/JHEP11(2013)181 [arXiv:1306.3926 [hep-ph]].

[11] C. T. Lu, J. Chang, K. Cheung and J. S. Lee, JHEP **1508**, 133 (2015) doi:10.1007/JHEP08(2015)133 [arXiv:1505.00957 [hep-ph]].

[12] A. J. Barr, M. J. Dolan, C. Englert and M. Spannowsky, Phys. Lett. B **728** (2014) 308 doi:10.1016/j.physletb.2013.12.011

[arXiv:1309.6318 [hep-ph]]: M. J. Dolan, C. Englert, N. Greiner and M. Spannowsky, Phys. Rev. Lett. **112** (2014) 101802 doi:10.1103/PhysRevLett.112.101802 [arXiv:1310.1084 [hep-ph]]; F. Bishara, R. Contino and J. Rojo, arXiv:1611.03860 [hep-ph]; M. J. Dolan, C. Englert, N. Greiner, K. Nordstrom and M. Spannowsky, Eur. Phys. J. C **75** (2015) no.8, 387 doi:10.1140/epjc/s10052-015-3622-3 [arXiv:1506.08008 [hep-ph]]; J. K. Behr, D. Bortoletto, J. A. Frost, N. P. Hartland, C. Issever and J. Rojo, Eur. Phys. J. C **76** (2016) no.7, 386 doi:10.1140/epjc/s10052-016-4215-5 [arXiv:1512.08928 [hep-ph]]; V. Martn Lozano, J. M. Moreno and C. B. Park, JHEP **1508** (2015) 004 doi:10.1007/JHEP08(2015)004 [arXiv:1501.03799 [hep-ph]]; Q. H. Cao, Y. Liu and B. Yan, Phys. Rev. D **95** (2017) no.7, 073006 doi:10.1103/PhysRevD.95.073006 [arXiv:1511.03311 [hep-ph]]; S. Di Vita, C. Grojean, G. Panico, M. Riembau and T. Vantalon, JHEP **1709** (2017) 069 doi:10.1007/JHEP09(2017)069 [arXiv:1704.01953 [hep-ph]]; A. Adhikary, S. Banerjee, R. K. Barman, B. Bhattacherjee and S. Niyogi, arXiv:1712.05346 [hep-ph]; J. H. Kim, Y. Sakaki and M. Son, arXiv:1801.06093 [hep-ph].
[13] S. Homiller and P. Meade, arXiv:1811.02572 [hep-ph].
[14] See T. Plehn, M. Spira and P. M. Zerwas in Ref. [4].
[15] D. de Florian and J. Mazzitelli, JHEP **1509**, 053 (2015) doi:10.1007/JHEP09(2015)053 [arXiv:1505.07122 [hep-ph]].
[16] R. Frederix, S. Frixione, V. Hirschi, F. Maltoni, O. Mattelaer, P. Torrielli, E. Vryonidou and M. Zaro, Phys. Lett. B **732** (2014) 142 doi:10.1016/j.physletb.2014.03.026 [arXiv:1401.7340 [hep-ph]].
[17] J. Baglio, A. Djouadi, R. Grber, M. M. Mhlleitner, J. Quevillon and M. Spira, JHEP **1304**, 151 (2013) doi:10.1007/JHEP04(2013)151 [arXiv:1212.5581 [hep-ph]].
[18] D. de Florian *et al.* [LHC Higgs Cross Section Working Group], doi:10.23731/CYRM-2017-002 arXiv:1610.07922 [hep-ph].
[19] *Higgs Cross Section Working Group*, https://cern.ch/twiki/bin/view/LHCPhysics/LHCHXSWG.
[20] R. Contino *et al.*, CERN Yellow Report, no. 3, 255 (2017) doi:10.23731/CYRM-2017-003.255 [arXiv:1606.09408 [hep-ph]].
[21] M. Vos, "Top physics beyond the LHC," arXiv:1701.06537 [hep-ex].
[22] M. Czakon and A. Mitov, Comput. Phys. Commun. **185**, 2930 (2014) doi:10.1016/j.cpc.2014.06.021 [arXiv:1112.5675 [hep-ph]].
[23] K. Melnikov, M. Schulze and A. Scharf, Phys. Rev. D **83**, 074013 (2011) doi:10.1103/PhysRevD.83.074013 [arXiv:1102.1967 [hep-ph]].
[24] J. Alwall *et al.*, JHEP **1407**, 079 (2014) doi:10.1007/JHEP07(2014)079 [arXiv:1405.0301 [hep-ph]].
[25] P. Nason, JHEP **0411**, 040 (2004) doi:10.1088/1126-6708/2004/11/040 [hep-ph/0409146]; S. Frixione, P. Nason and C. Oleari, JHEP **0711**, 070 (2007) doi:10.1088/1126-6708/2007/11/070 [arXiv:0709.2092 [hep-ph]]; S. Alioli, P. Nason, C. Oleari and E. Re, JHEP **1006**, 043 (2010) doi:10.1007/JHEP06(2010)043 [arXiv:1002.2581 [hep-ph]].
[26] T. Sjstrand *et al.*, Comput. Phys. Commun. **191**, 159 (2015) doi:10.1016/j.cpc.2015.01.024 [arXiv:1410.3012 [hep-ph]].
[27] C. Degrande, C. Duhr, B. Fuks, D. Grellscheid, O. Mattelaer and T. Reiter, Comput. Phys. Commun. **183**, 1201 (2012) doi:10.1016/j.cpc.2012.01.022 [arXiv:1108.2040 [hep-ph]].
[28] V. Hirschi and O. Mattelaer, JHEP **1510**, 146 (2015) doi:10.1007/JHEP10(2015)146 [arXiv:1507.00020 [hep-ph]].
[29] P. Artoisenet, R. Frederix, O. Mattelaer and R. Rietkerk, JHEP **1303**, 015 (2013) doi:10.1007/JHEP03(2013)015 [arXiv:1212.3460 [hep-ph]].
[30] ATLAS Collaboration, Study of the double Higgs production channel H($\rightarrow$ bb)H($\rightarrow$gamma gamma) with the ATLAS experiment at the HL-LHC, ATL-PHYS-PUB-2017-001, 2017, url: http://cds.cern.ch/record/2243387.
[31] J. de Favereau *et al.* [DELPHES 3 Collaboration], JHEP **1402**, 057 (2014) doi:10.1007/JHEP02(2014)057 [arXiv:1307.6346 [hep-ex]].
[32] ATLAS Collaboration, Expected performance for an upgraded ATLAS detector at High-Luminosity LHC, ATL-PHYS-PUB-2016-026, 2016, url: http://cds.cern.ch/record/2223839.
[33] ATLAS Collaboration, Expected performance of the ATLAS b-tagging algorithms in Run-2, ATL-PHYS-PUB-2015-022, July 24, 2015.
[34] R. D. Ball *et al.* [NNPDF Collaboration], JHEP **1504** (2015) 040 doi:10.1007/JHEP04(2015)040 [arXiv:1410.8849 [hep-ph]].
[35] J. Pumplin, D. R. Stump, J. Huston, H. L. Lai, P. M. Nadolsky and W. K. Tung, JHEP **0207** (2002) 012 doi:10.1088/1126-6708/2002/07/012 [hep-ph/0201195].
[36] H. L. Lai, M. Guzzi, J. Huston, Z. Li, P. M. Nadolsky, J. Pumplin and C.-P. Yuan, Phys. Rev. D **82** (2010) 074024 doi:10.1103/PhysRevD.82.074024 [arXiv:1007.2241 [hep-ph]].
[37] ATLAS Collaboration, "Calibration of the performance of *b*-tagging for *c* and light-flavour jets in the 2012 ATLAS data," ATLAS-CONF-2014-046, July 3, 2014.
[38] https://twiki.cern.ch/twiki/bin/view/LHCPhysics/HiggsEuropeanStrategy
[39] A. J. Barr, M. J. Dolan, C. Englert, D. E. Ferreira de Lima and M. Spannowsky, JHEP **1502**, 016 (2015) doi:10.1007/JHEP02(2015)016 [arXiv:1412.7154 [hep-ph]].
[40] F. Kling, T. Plehn and P. Schichtel, Phys. Rev. D **95** (2017) no.3, 035026 doi:10.1103/PhysRevD.95.035026 [arXiv:1607.07441 [hep-ph]].
[41] S. Borowka, N. Greiner, G. Heinrich, S. P. Jones, M. Kerner, J. Schlenk, U. Schubert and T. Zirke, Phys. Rev. Lett. **117** (2016) no.1, 012001 Erratum: [Phys. Rev. Lett. **117** (2016) no.7, 079901] doi:10.1103/PhysRevLett.117.079901, 10.1103/PhysRevLett.117.012001 [arXiv:1604.06447 [hep-ph]].
[42] S. Borowka, N. Greiner, G. Heinrich, S. P. Jones, M. Kerner, J. Schlenk and T. Zirke, JHEP **1610** (2016) 107 doi:10.1007/JHEP10(2016)107 [arXiv:1608.04798 [hep-ph]].
[43] M. Grazzini, G. Heinrich, S. Jones, S. Kallweit, M. Kerner, J. M. Lindert and J. Mazzitelli, JHEP **1805** (2018) 059 doi:10.1007/JHEP05(2018)059 [arXiv:1803.02463 [hep-ph]].
[44] F. Maltoni, E. Vryonidou and M. Zaro, JHEP **1411** (2014) 079 doi:10.1007/JHEP11(2014)079 [arXiv:1408.6542 [hep-ph]].
[45] S. Dulat *et al.*, Phys. Rev. D **93** (2016) no.3, 033006 doi:10.1103/PhysRevD.93.033006 [arXiv:1506.07443 [hep-ph]].

[46] M. L. Mangano, M. Moretti, F. Piccinini and M. Treccani, JHEP **0701** (2007) 013 doi:10.1088/1126-6708/2007/01/013 [hep-ph/0611129].
[47] J. Alwall *et al.*, Eur. Phys. J. C **53** (2008) 473 doi:10.1140/epjc/s10052-007-0490-5 [arXiv:0706.2569 [hep-ph]].